To the Graduate Council:

I am submitting herewith a dissertation written by W-L-Namila Chandula Liyanage entitled "Exploring Skyrmions Dynamics and Structure Using Neutron Scattering." I have examined the final paper copy of this dissertation for form and content and recommend that it be accepted in partial fulfillment of the requirements for the degree of Doctor of Philosophy, with a major in Physics.

Dustin A. Gilbert,, Major Professor

We have read this dissertation and recommend its acceptance:

Christian Batista

Joon Sue Lee

Haidong Zhou

Accepted for the Council:

Dixie L. Thompson

Vice Provost and Dean of the Graduate School

To the Graduate Council:

I am submitting herewith a dissertation written by W-L-Namila Chandula Liyanage entitled "Exploring Skyrmions Dynamics and Structure Using Neutron Scattering." I have examined the final electronic copy of this dissertation for form and content and recommend that it be accepted in partial fulfillment of the requirements for the degree of Doctor of Philosophy, with a major in Physics.

Dustin A. Gilbert,, Major Professor

We have read this dissertation
and recommend its acceptance:

Christian Batista

Joon Sue Lee

Haidong Zhou

Accepted for the Council:

Dixie L. Thompson

Vice Provost and Dean of the Graduate School

(Original signatures are on file with official student records.)

Exploring Skyrmions Dynamics and Structure Using Neutron Scattering

A Dissertation Presented for the

Doctor of Philosophy

Degree

The University of Tennessee, Knoxville

W-L-Namila Chandula Liyanage

August 2023

To my mother Sumithra, father Upali and wife Peshadi

Acknowledgements

I would like to take this opportunity to express my sincere gratitude and appreciation to all the individuals who have played a significant role in the completion of this PhD thesis. The journey of my PhD has been a transformative experience, filled with invaluable lessons. Through this remarkable endeavor, I have not only acquired profound subject knowledge, honed my skills as a researcher, and mastered the art of effectively communicating complex ideas, but I have also discovered my own strengths and unwavering perseverance.

First and foremost, I am deeply indebted to my supervisor, Prof. Dustin Gilbert, whose guidance, expertise, and unwavering support have been invaluable throughout this research endeavor. His insightful feedback, constant encouragement, and dedication to my academic growth have shaped me into a better researcher.

I am grateful to the members of my thesis committee, Prof. Christian Batista, Prof. Joon Sue Lee, and Prof. Haidong Zhou, for their valuable time, expertise, and constructive criticism. Their expertise in their respective fields has greatly enriched the quality of this work.

I would like to extend my heartfelt appreciation to the faculty members and researchers at The University of Tennessee, Knoxville who have contributed to my intellectual development. Their knowledge-sharing, thought-provoking discussions, and collaborative spirit have been instrumental in shaping my research perspective.

Furthermore, I would like to express my gratitude to my colleagues and lab mates, Nan Tang, Cameron Jorgenson, Lizzie, Corrissa who have been an incredible source of inspiration, and support. Their valuable insights, technical assistance, and engaging discussions have enhanced the research experience and made it more enriching.

I am deeply thankful to DOE, that have provided financial support for this research. Their generous contributions have allowed me to pursue my academic goals and dedicate myself fully to this endeavor.

During my Ph.D., I had the pleasure of conducting a series of experiments, which undoubtedly became the highlight of my graduate career. These invaluable experiences took place at esteemed facilities such as ORNL, and NIST. I consider myself incredibly fortunate to have collaborated with Julie A. Borchers, Marcus, Kathryn Krycka, Brian B. Maranvillw, Alexander J. Grutter at NIST, Lisa DeBeerSchmitt and Michael Fitzimmons at ORNL, whose guidance and expertise expanded my understanding of experiments to a great extent. I am truly grateful to each and every one of these scientists for their invaluable contributions.

I would also like to express my deepest appreciation to Sergio A. Montoya, Eric E. Fullerton from University of San Diego. I am sincerely grateful for their contributions and would like to acknowledge their significant role in the success of my work.

I am profoundly grateful to my beloved family, whose unwavering love, understanding, and support have been the cornerstone of my academic journey. To my incredible parents, my mother Sumithra and my late father Upali. I am forever indebted to you for instilling within me the profound value of education and for all the support and guidance. To my cherished wife, Peshadi, I am deeply grateful for your unwavering love, encouragement. Your presence by my side has been a motivation to push through difficult times and pursue my academic dreams with determination.

Last but not least, I am sincerely grateful to each and every person who has offered their support, guidance, and encouragement along the way.

Abstract

Magnetic skyrmions are topologically protected chiral spin textures with great potential for next-generation consumer technologies. These magnetic structures can be described as spins continuously wrapping into a closed coplanar loop, featuring a core and fencing perimeter with opposite out-of-plane orientations. While conventional depictions of magnetic skyrmions use a two-dimensional projection, recent research underscores the importance of their three-dimensional structure in determining their topology and stability. Magnetic skyrmions typically emerge just below the curie temperature of a magnetic material, creating what is known as a skyrmion pocket. In most materials the stability pocket is at low temperatures and finite fields, however recent studies have stabilized skyrmions in Fe/Gd ML systems under ambient conditions. The key to achieving enhanced stability in this system was the unique 3D structure of the skyrmion, consisting of both Néel-like and Bloch-like components along the length of the skyrmion tube. My first work focuses on experimentally determining the structure of these hybrid skyrmions using neutron scattering. To interpret the neutron data, micromagnetic simulations were conducted

and the simulated diffraction pattern calculated using a Born approximation. The resulting magnetic profile offers insights into the structure of the skyrmions, including the depth profile, thickness of the Bloch and Néel segments, and the core diameter. Beyond their primary structure as a topologically protected soliton, skyrmions often form ordered hexagonal lattices. While the nucleation and annihilation of single skyrmions is expected to be very fast, on the order of nanoseconds, recent works have suggested that the ordering of the skyrmion lattice is much slower. To investigate these slow dynamics, the formation and destruction time scales of skyrmion lattice were investigated using neutron scattering, performed on three different prototypical skyrmion materials: MnSi, $Fe_{0.85}Co_{0.15}Si$, and Cu_2OSeO_3. Using a step-like magnetic field to move the skyrmions into and out-of the stability pocket, the lattice ordering is captured using time resolved small-angle neutron scattering. Fitting the time-dependent diffraction data, the slow timeframes were confirmed, with ordering occurring in 10-100 ms. The formation and destruction times were shown to depend on the magnitude of the field strep, the temperature, the magnetic anisotropy, and the saturation magnetization.

Table of Contents

1 Introduction **1**

1.1 Introduction 1

1.2 Magnetic Domains 2

1.3 Magnetic Spin Configuration and Skyrmions 2

1.4 Skyrmion Materials 6

1.5 Formation of skyrmion lattice 9

1.6 Dipole stabilized skyrmions 10

2 Methods and Materials **12**

2.1 Neutron Scattering 12

2.2 Neutron Reflectometry 15

2.3 Polarized Neutron Reflectometry (PNR) 19

2.4 GISANS 23

2.5 Vibrating Sample Magnetometry (VSM) 23

2.6 Object-Oriented Micromagnetic Framework 25

2.7 Samples 27

3 Three-Dimensional Structure of Hybrid Magnetic Skyrmions Determined by Neutron Scattering 30
3.1 Introduction 30
3.2 Experimental Procedure 34
3.2.1 Results 38

4 Skyrmion lattice formation and destruction mechanisms probed with SANS 61
4.1 Introduction 61
4.2 Methods 63
4.3 Results 65
4.3.1 MnSi 65
4.3.2 $Fe_{0.85}Co_{0.15}Si$ 73
4.3.3 Cu_2OSeO_3 78
4.4 Discussion 79
4.4.1 Conclusion 88

5 Conclusions 90

Bibliography 92

Appendix 106

A Supplemental Materials For Neutron Scattering and Reflectometry 106
A.1 Scattering Length 106

A.2 Differential Cross Section 108

A.3 Magnetic Scattering 110

A.4 Polarized Neutron Reflectometry (PNR) 112

A.4.1 Magnetic Dependent Reflectometry 114

B Supplemental Materials For Chapter 3 **116**

B.1 Hystersis Loop Data For FeGd ML System 116

Appendix **106**

Vita **118**

List of Tables

4.1 Summary of the formation and destruction time constants with uncertainties for three samples. These data contains values for larger field steps. 81

4.2 Saturation magnetization, exchange stiffness, DMI constant values for each of the sample and the interskyrmion distance (skyrmion lattice size). SM = semimetallic, Insul=insulator. 85

List of Figures

1.1 Bloch and Néel domain walls. (a) Bloch wall, with moments (red arrows) rotating in the plane perpendicular to the domain wall. (b) Néel type domain wall with moments rotating in the plane normal to the domain wall 3

1.2 Two main type skyrmions (a) Néel-type skyrmions (b) Bloch type skyrmions [1] 5

1.3 Magnetic field - temperature diagram for MnSi [2]. Small skyrmion pocket near the curie temperature initially known as the ‘Anomalous’ phase 8

2.1 Schematic of Very small-angle neutron scattering (vSANS) instrument at NIST Center for Neutron Research (NCNR). In the image, the tan, rectangular region is for beam conditioning and collimation, while the green tube houses the detectors to capture the scattering. The sample sits between the tan and the green. 13

2.2 Typical neutron scattering experiment. A magnetic field (red arrow) is applied parallel to the neutron beam. 16
2.3 SANS experiment setup for skyrmion material. The hexagonal pattern can be observed in the SANS detector. 17
2.4 Diagram of Reflectometry configurations (a) Specular reflections from layered structure. The incident angle equals the reflected angle. (b) Off-specular reflections due to in-plane structure. Q is the momentum transfer vector. 18
2.5 Four reflected cross sections spin (a) up-up (b) down-down (c) up-down (d) down-up 20
2.6 Schematic of the GISANS experiment setup. The diagram shows the sample illuminated at grazing incidence, with the specular (red arrow) and off-specular reflection (orange) scattering indicated. 22
2.7 Dynacool PPMS at Gilbert lab 24
2.8 Fe-Gd ML system with Ta as capping and seed layer. 29
3.1 Schematic of flux closure domains. Red lines represent magnetic field lines, and blue arrows represent Néel caps in the sample. [3] 32
3.2 (a) Measured stripe state data for Fe/Gd ML showing two diffraction peaks. (b) Measured SANS pattern for the skyrmion state. 37

3.3 (a) Specular reflectivity measurement and (b) converged depth profile for the Gd/Fe multilayer in the saturated state (in-plane saturation, 500 mT). The neutron polarization axis is in-plane and parallel to the saturating field in this scattering configuration. Only the non-spin-flip data are shown since there is no appreciable spinflip signal in saturation. (c) Specular reflectometry and (d) converged depth profile measured in a 1-mT field, in the skyrmion state with the magnetic surface state emphasized in (e). For (a), the neutron polarization axis is in the plane of the film, while for (c), the neutron polarization axis is out-of-plane and parallel to the small guide field. 40

3.4 Grazing-incidence small-angle neutron scattering (GISANS) data in (a) the stripe state, (b) skyrmion state, and (c) saturated state. The z contrast uses a logarithmic scale. For all three measurements, the specular peak appears at $Q_y = 0$, while the off-specular peaks appear at $Q_y = \pm 0.00338$ Å^{-1} and ± 0.0025 Å^{-1} for the stripe and skyrmion states, respectively. 44

3.5 Integrated intensity of the specular reflection from GISANS for the skyrmion (triangle), out-of-plane saturated states (circle), and theory from the Refl1d model (line) 46

3.6 Integrated intensity from the off-specular diffraction peak from GISANS (circle) and theoretical results from micromagnetic modeling (line). . 47

3.7 (a) Plane view image of the simulated skyrmion lattice. (b)-(f) Slices of the magnetic configuration taken along the length of the skyrmion tube, with (b) Z=16 nm corresponding to the top surface and an inward wrapping Néel cap, (d) Z=59 nm corresponding to the middle and a clockwise Bloch type, and (f) Z=101 nm corresponding to the bottom surface and an outward wrapping Néel cap. 50
3.8 (a) The in-plane width of the skyrmion boundary region. (b) The total in-plane magnetization from OOMMF integrated versus depth and compared to the magnetic SLD profile from the PNR results. (c) The in-plane angle of the skyrmion boundary region versus depth, with +90°/0/-90° corresponding to inward Néel, clockwise Bloch, and outward Néel, respectively. Note that 0○ is defined as the azimuthal direction. 51
3.9 Calculated 2D transmission SANS from simulation 54
3.10 (a) grazing-incidence SANS(GISANS) measurements simulated at Q_z = -0.031 Å^{-1} (b) cumulative GISANS pattern from the OOMMF simulations of the skyrmion state. The z-contrast uses a logarithmic scale. The cumulative GISANS pattern is the sum of all measured theta angles (i.e., all measured Q_z values), while the experimental results are measured at sequential angles, analogous to panel (a) and Fig. 3.4b. 55

3.11 Average non-spin-flip specular reflectivity <R++,R−−> and spin-flip reflectivity <R+−,R−+> from PNR, OOMMF (1D depth profile) and three-dimensional micromagnetic simulation (OOMMF, shown in Fig. 3.7) at $Q_y = 0$. A constant background was added to the three-dimensional OOMMF model. 58

4.1 Experiment setup in vSANS instrument (a) sample (MnSi) attached to the sample holder. (b) sample holder attached to the cryogenic cold head. 64

4.2 The B-T phase diagram for MnSi [11] was examined in this experiment. The field was incrementally increased to push the skyrmion lattice out or into the stabilized window, leading to its destruction (indicated by the red arrow) or creation (indicated by the blue arrow), respectively. Each measurement involved step 1, where the field was increased (decreased) following the red arrow, and step 2, where the field was subsequently decreased (increased) following the blue arrow in the B-T phase diagram. 66

4.3 (a) The 2D small-angle neutron scattering (SANS) pattern obtained from the MnSi sample revealed a hexagonal scattering pattern at (3.8) $\times 10^{-2}$ Å^{-1}, corresponding to a skyrmion lattice size of 165 Å. The magnetic field used during the measurement was 237.5 mT. (b) In the conical phase of the MnSi sample, which is outside the skyrmion stabilized window, the hexagonal SANS pattern disappeared from the detector. 68

4.4 exponential functions used to fit the data for (a) destruction (b) formation of skrmion lattice. 70

4.5 The graph illustrates the normalized averaged scattering intensity in the azimuthal direction of the scattering pattern plotted against time for the destruction and construction of the skyrmion lattice. 72

4.6 SANS data for FCS sample (a) Ring type scattering pattern is visible in the detector. (b) Scattering for sample in the conical phase (c) At lower boundary 2D SANS pattern shows a hexagon imposed over a uniform ring (d) At lower boundary out of skyrmion stabilizing envelope weak diffraction peaks are observed along the Qy direction 75

4.7 The graph illustrates the normalized averaged scattering intensity in the azimuthal direction of the scattering pattern plotted against time for (a) the formation and (b) destruction of the skyrmion lattice. . . . 76

4.8 SANS patterns of Cu_2OSeO_3 taken at (a) 23 mT field and (b) 43 mT field Graphs depicting the normalized averaged scattering intensity in the azimuthal direction over time, illustrating (c) the formation and (d) destruction of the skyrmion lattice. 80
4.9 Example trends, taken from MnSi at 28.8 K and a field step of 287.5 mT to 212.5 mT, corresponding to lattice formation and showing (a) the peak position and (b) width in q and (c) the peak width in the azimuthal direction. 83

A.1 (a) momentum transfer vetor in terms of incident and scattered wavevector (b) A plane wave of neutrons travelling in z direction and scattered uniformally from a stationary nuclei and scatter in radial direction. 109
A.2 (a) Dipole field generated from an unpaired electron (dashed lines). μ_e is the moment of the electron and μ_n is the moment associated with neutron (b) Schematic of spin of electron and its component perpendicular to the maomentum transfer vector (Q). adapted from (article)[4] 111

B.1 The Fe/Gd ML system was characterized by measuring the magnetic moment vs field data. The sample was first saturated by applying a field of 500 mT at 45 degrees with respect to the out-of-plane (OOP) direction. Then the field was decreased, as indicated by the red arrow, until zero field (remanence) was reached, at which point a stripe state is formed (as evidenced by two diffraction peaks in the SANS detector). Subsequently, the field was increased to 190 mT in the OOP direction, as indicated by the black 117

Chapter 1

Introduction

1.1 Introduction

Humans have used magnetic materials for more than centuries, even before recorded history began. The writing of Thales, Geek, recorded the power of magnetic loadstone (a naturally occurring stone comprised of Fe_3O_4) as long ago 600 BC, and the Chinese had used compass sometime before 2500 BC.

Scientific understanding of magnetism and magnetic materials accelerated in the second millennium AD, starting with the discovery of magnetic poles by P. Peregrines in 1269 AD. In 1819 Hans Christian Orsted (often spelled Oersted) (1777–1851) observed the force exerted on a magnetic needle by the electric current in a nearby wire, coupling charge currents to magnetic fields[5]. In 1865 Maxwell formally unified the fields of magnetism and electrostatics (including currents) in his electromagnetic theory, one of the most outstanding achievements in physics. Many scientists have contributed to the field of magnetism and developed technologies predicated on magnetic phenomenon and materials, impacting energy, transport, telecommunications, information technologies, navigation, and medicine, among others.

1.2 Magnetic Domains

In a ferromagnetic material, the magnetic moments tend to align parallel with their neighbors; collections of many spins with parallel alignment are called magnetic domains. The theory behind magnetic domains was introduced by French physicist Weiss in 1906 [6]. The boundary between two domains with different orientations is called the domain wall. There are different types of domain walls defined by how the magnetic moments rotate between the domains. Two main types of domain walls exist: for Bloch walls, named after Felix Bloch, the magnetic moments rotate in the plane parallel to the domain wall as shown in Figure 1.1(a). For a Néel-type domain wall, named after Louis Néel, the magnetic moments rotate in the plane normal to the domain wall, as shown in Figure 1.1(b).

1.3 Magnetic Spin Configuration and Skyrmions

One way to categorize magnetic spin configurations is to label them as colinear or non-colinear. In a colinear magnetic system, neighboring spins prefer to align parallel or antiparallel (ferro- and antiferromagnetism), while non-colinear magnetic systems

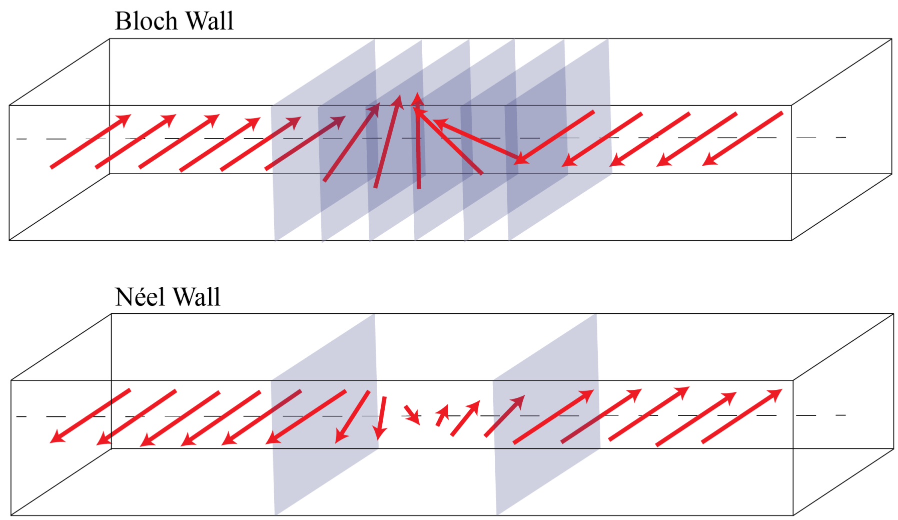

Figure 1.1: Bloch and Néel domain walls. (a) Bloch wall, with moments (red arrows) rotating in the plane perpendicular to the domain wall. (b) Néel type domain wall with moments rotating in the plane normal to the domain wall

tend to have a tilt between their alignment usually due to competition between magnetic energy terms. My research focuses on a specific non-colinear magnetic system called skyrmions. Skyrmions are a whirl of spin configuration in-which the magnetic moments form continuous, closed loops, analogous to a small domain with the condition that the domain wall is continuous and has no kinks or twists. The idea of the skyrmion was first introduced by British scientist Tony Hilton Royle Skyrme, who used to describe a nuclear model for low energy dynamics between mesons and baryons [7, 8].

The structure of a skyrmion in a magnetic material can be explained as a continuous co-planar wrapping of magnetic moments, with a core and fencing perimeter pointing out of the plane, with opposite orientations. Analagous to the domain walls discussed above, skyrmions have two configurations, shown in Fig. 1.2. For Néel-type skyrmions, the magnetic spins rotate along the radial direction, perpendicular to the domain boundaries as they move away from the core (Fig. 1.2(a)). In Bloch type skyrmions, the magnetic spins rotate through the azimuthal direction, parallel to the domain boundary, as it moves away from the core (Fig 1.2(b)).

These magnetic structures are topologically protected such that they cannot be continuously created or destroyed by using a field sequence; the saturated magnetic configuration is a different (topologically trivial) state. Furthermore, these structures also tend to be stable in a limited temperature\magnetic field parameter space. Usually, skyrmions self-organize into a 2D hexagonal lattice called a skyrmion lattice.

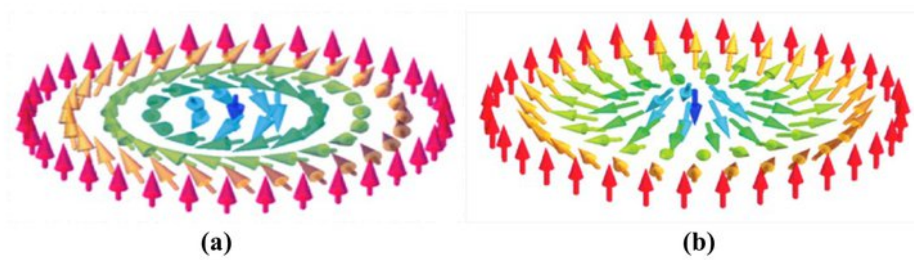

Figure 1.2: Two main type skyrmions (a) Néel-type skyrmions (b) Bloch type skyrmions [1]

The small size of the skyrrmion (usually <100 nm in diameter), high packing density and topological protection makes the skyrmion suitable for magnetic data storage. In addition to the topological properties of the skyrmion, they can be moved or excited using electrical currents; these current densities are much smaller than analogous domain-wall based systems. The driving of skyrmions using charge currents can be explained using the spin-transfer torque (STT) effect [9]. Due to these exciting properties, skyrmions are suitable for low-powered electronic devices [10, 1].

1.4 Skyrmion Materials

Skyrmions were reported for the first time in the magnetic material MnSi, as evidenced by neutron scattering performed in 2009 by Mühlbauer *et al.*[2]. MnSi in this system forms a crystallized B20 structure which lacks inversion symmetry and belongs to the P_{213} space group [11]. Since this discovery, there has been significant interest in magnetic skyrmions due to their exciting physics and potential for device application. Subsequently, more magnetic skyrmion materials have been discovered, including FeCoSi, Cu_2OSeO_3, and FeGe, among others.

For example, skyrmion lattice has been found in $Fe_xCo_{1-x}Si$ at x=0.2,temperatures of 22-30 K and magnetic fields of 20-60 mT [12, 13].Skyrmions have also been found in multiferroic materials such as Cu_2OSeO_3 [14, 15]. It has been found that the stabilizing temperature is around 57.4 K. Interestingly, this material shows a multidomain skyrmion lattice [16]. This material is also one of the few insulating skyrmion materials, making it especially attractive for inclusing in hybrid skyrmion-electronic applications. The B20 structure lacks inversion symmetry, resulting in a non-colinear interaction, which foments the creation of magnetic helical and conical phases throughout the temperature\field parameter space below the Curie temperature. However, near the Curie temperature, the thermal contributions motivate the formation of skyrmions in a small pocket, previously known as the 'A' phase or the 'Anomalous' phase [17, 17]; this phase is shown in the magnetic field-temperature (B-T) phase diagram for MnSi, Figure 1.3. This anomalous phase was later associated with the stability of magnetic skyrmions.

While skyrmions can readily form in B20 materials such as MnSi, they are stable only in a small pocket in the phase diagram, usually far below room temperature and in a finite magnetic field. As a result, it is challenging to integrate these skyrmions with other spintronic devices or broadly deploy them for consumer technologies. To realize deployable, skyrmion-based technologies it is necessary to broaden the skyrmion stability envelope to include ambient conditions, e.g. at or near room temperature and zero magnetic field.

One promising material was reported in 2011 by Yu.*et al,* who discovered skyrmions in B20 structured FeGe thin films between 260 K and 280 K.[18, 19]. While this temperature range is still below room temperature, it is a promising first step towards room temperature stable skyrmions.

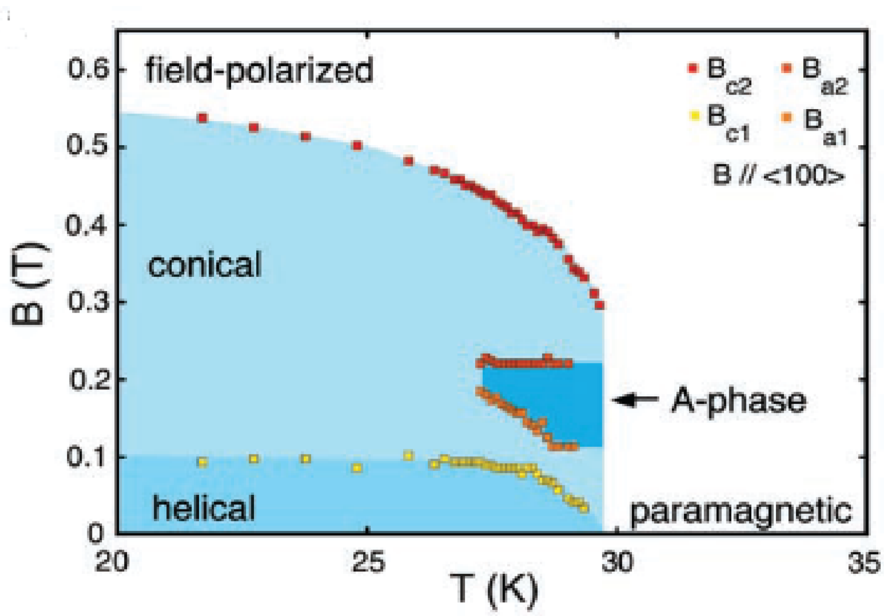

Figure 1.3: Magnetic field - temperature diagram for MnSi [2]. Small skyrmion pocket near the curie temperature initially known as the 'Anomalous' phase .

1.5 Formation of skyrmion lattice

Early studies of skyrmion materials proposed that the Dzyaloshinskii-Moriya interaction (DMI) was necessary to realize the winding of the skyrmions. The DMI interaction is an antisymmetric exchange interaction that takes the form of $D \cdot (\bar{S_1} \times \bar{S_2})$ where D is the DMI constant and and $\bar{S_1}$ and $\bar{S_2}$ are the vector orientations of two neighboring spins[17, 20]. This cross-product motivates a 90° alignment with a handedness (or direction of winding) wich is uniform across the sample.

Another more common, type of magnetic interaction is the exchange interaction which extends to a few atomic thicknesses and favors aligning spins parallel or antiparallel to each other; this interaction is responsible for ferro and antiferromagnetic configurations. The exchange interaction takes the form of $J \cdot (\bar{S_1} \cdot \bar{S_2})$ and J is the exchange constant. For a ferromagnetic material J is negative and neighboring spins align parallel to each other, while for an antiferromagnetic material J is positive and spins align antiparallel to each other.

A third energy term is the Zeeman energy, which couples the magnetic moments to an applied magnetic field: $-\bar{M} \cdot \bar{H}$. The Zeeman energy is minimized when spins are parallel to the external magnetic field.

The competition between the DMI and exchange interactions results in a gentle and continuous curling of the magnetization, eventually forming a closed loop termed the Skyrmion.[21, 22, 23] In systems which use the DMI to stabalize skyrmions, since the DMI has a handedness the wrapping of each skyrmion is in the same direction. Once assembled into a hexagonal lattice, the magnetic configuration can alternatively be presented as an assembly of three helices, arranged with 120° relative orientation.

1.6 Dipole stabilized skyrmions

As mentioned earlier, realizing skyrmions which are stable near room temperature necessary to achieving a deployable consumer technology. Recently our group has demonstrated the realization of magnetic skyrmions that are stable in ambient conditions (room temperature and zero magnetic field)[3].

Desautels *et al.* demonstrated the formation of an ordered skyrmion lattice in amorphous Fe/Gd thin-film multilayers stabilized through dipole interactions [3]. By applying a unique magnetic field sequence, the spin configuration was transformed from the saturated state to artificially ordered stripe domains. From the stripe configuration an out-of-plane magnetic field is applied, causing the stripe domains to pinch and form an ordered skyrmion lattice. Once generated, these skyrmions were shown to be stable in the temperature range from <10 K – 320 K and 200 mT to -55 mT magnetic field range.

The improved stability of these skyrmions is a consequence of their stabilization mechanics and structure - which are both distinctly different from the skyrmions in B20 materials. In the Gd/Fe multilayer system, the magnetic skyrmions are stabilized by dipolar fields, with the regions between the skyrmions generating dipolar fields parallel to the skyrmion core, facilitating stability. These skyrmions also are proposed to have a unique structure, with flux-closure domains located at the surfaces of the film (coincident with the end of the skyrmion tubes). These flux closure domains are topologically identical to a Néel-type skyrmion. Between these flux-closure domains (Néel caps), the skyrmion tube forms a Bloch-type skyrmion. The direction of the winding of the Néel caps (radially inward or outward) follows the direction of the dipole field and so is opposite on the top and bottom film surfaces. Since the cores of the skyrmions are all precipitated from the stripe domains which are pinched as the magnetic field is applied, they share a common core direction. The common core and winding direction between all the skyrmions means that the chirality of the Néel-like component is the same for every skyrmion. Attempts to image these multi-component 'Hybrid' skyrmions with Lorentz transmission electron microscopy (LTEM) show that these skyrmions possess a Bloch-type structure with no long-range chirality control [24]. It is challenging to resolve Néel skyrmions with LTEM, and furthermore, the stacking of opposite chirality Néel skyrmions would result in near perfect cancellation of the signal. Thus, the LTEM result support the Néel/Bloch/Néel trilayer stacked skyrmion structure.

With both the topology and stability coupled to the structure, it is crucial to experimentally deterime the magnetic configuration of these skyrmions. In this research, neutron scattering techniques were used to investigate the three-dimensional structure of the hybrid skyrmion.

Chapter 2

Methods and Materials

2.1 Neutron Scattering

The neutron is a sub atomic particle with no net charge with magnetic moment and was first discovered in 1932 by Chadwick.[25, 26] Since its discovery the neutron has been used for various research purposes. Nowadays, neutron scattering is one of the popular technique to study magnetic nanostructres and magnetic properties in magnetic materials.[27] Generally, neutrons can be produced either spallation or fission.[26] Neutrons generated by above mentioned sources, termed hot neutrons, but their energy is quickly reduced through scattering with a moderator (usually contains water or D_2O or graphite) to become thermal or even cold neutrons (which have much lower energy). The De Broglie wavelength 2.1 and energy 2.2 assosiated with a neutron can be calculated by following equations,[27, 26] where m_n is the mass

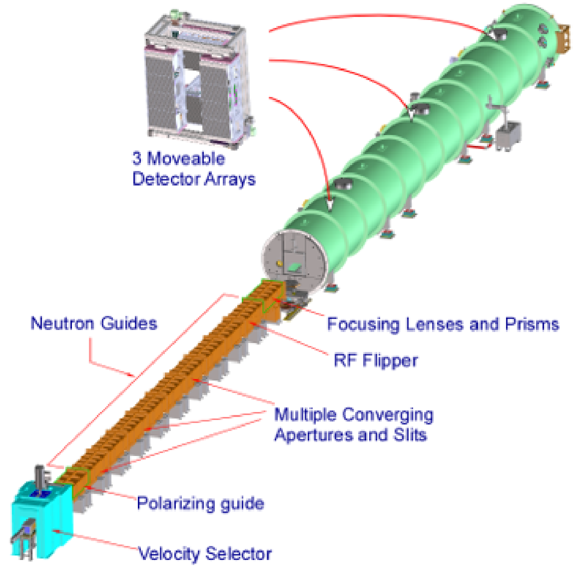

Figure 2.1: Schematic of Very small-angle neutron scattering (vSANS) instrument at NIST Center for Neutron Research (NCNR). In the image, the tan, rectangular region is for beam conditioning and collimation, while the green tube houses the detectors to capture the scattering. The sample sits between the tan and the green.

of the neutron and v is the velocity of the neutron and λ is the associated de Broglie wavelength. For an example neutrons with 14 Åhas the energy of 0.41 meV.

$$\lambda = \frac{h}{m_n v} \tag{2.1}$$

$$E = \frac{1}{2} m_n v^2 \tag{2.2}$$

More details about neutron scattering is discussed in the appendix.

One of the common approaches to neutron scattering is to illuminate a sample with a beam of monochromatic neutrons and observing the diffraction pattern as the neutrons (treated as a wave) interact with the sample. These techniques generate data in reciprocal space e.g. as the Fourier transform of the real space structure of the real space structure, rather than real-space. Since the neutron has a magnetic spin moment, this diffraction pattern can also encode magnetic structure. Using various neutron scattering instruments, the magnetic and nuclear structure can be determined for structures over a range from $\approx 10^{-10}$-10^{-6}m. Furthermore, the ability to perform energy analysis (spectroscopy) and the highly penetrating nature of neutrons (allowing sub surface investigations), combined with the aforementioned benefits, make neutron scattering an extremely useful tool in studying magnetism in condensed matter physics. Neutron scattering has been the gold standard for observing the skyrmion lattice. Other methods to observe the skyrmion lattice includes Lorentz transmission electron microscopy (LTEM), which reveals the magnetic structure in real space [21, 28]. Among the neutron scattering techniques, small-angle neutron scattering (SANS) is the appropriate technique to access 10's – 100's of nanometer-scale magnetic structures, including skyrmions. Among the different SANS instruments, the very small-angle neutron scattering (vSANS) instrument at the NIST Center for Neutron Research (Fig. 2.1) has an appropriate range to measure our hybrid skyrmions.

An example SANS experiment setup is shown in Fig. 2.2. In this example the incident neutron beam and magnetic field are aligned parallel and illuminate the sample in a transmission geometry. After the neutron beam passes through the sample, a scattering pattern can be observed in the detector.

Since the skyrmion lattice is hexagonally ordered, the diffraction pattern, which is the Fourier transform of the real-space structure is a hexagon, which is captured on the SANS detector (Fig. 2.3). The resultant scattering pattern is a combination of structure and form factors, which arise from the structure of the skyrmion lattice and the skyrmion itself, respectively. We can calculate the structure factor related to the skyrmion lattice size by analyzing the detector's scattering pattern.

2.2 Neutron Reflectometry

Neutron reflectometry is a method in which a neutron beam illuminates the flat surface of a sample at grazing incidence, resulting in thin-film diffraction which

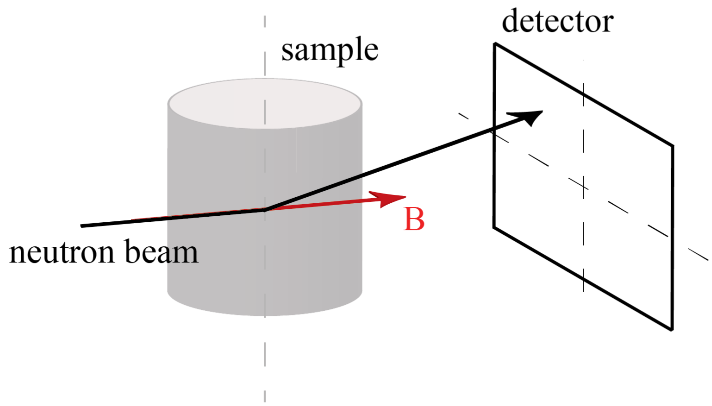

Figure 2.2: Typical neutron scattering experiment. A magnetic field (red arrow) is applied parallel to the neutron beam.

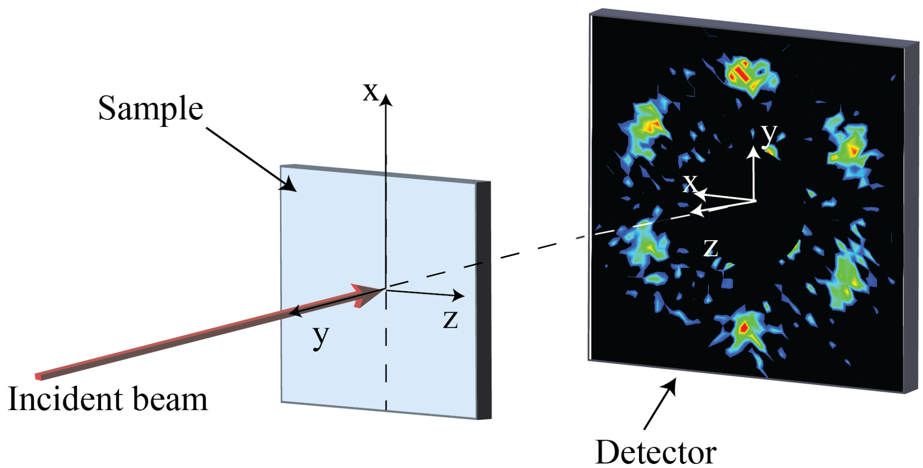

Figure 2.3: SANS experiment setup for skyrmion material. The hexagonal pattern can be observed in the SANS detector.

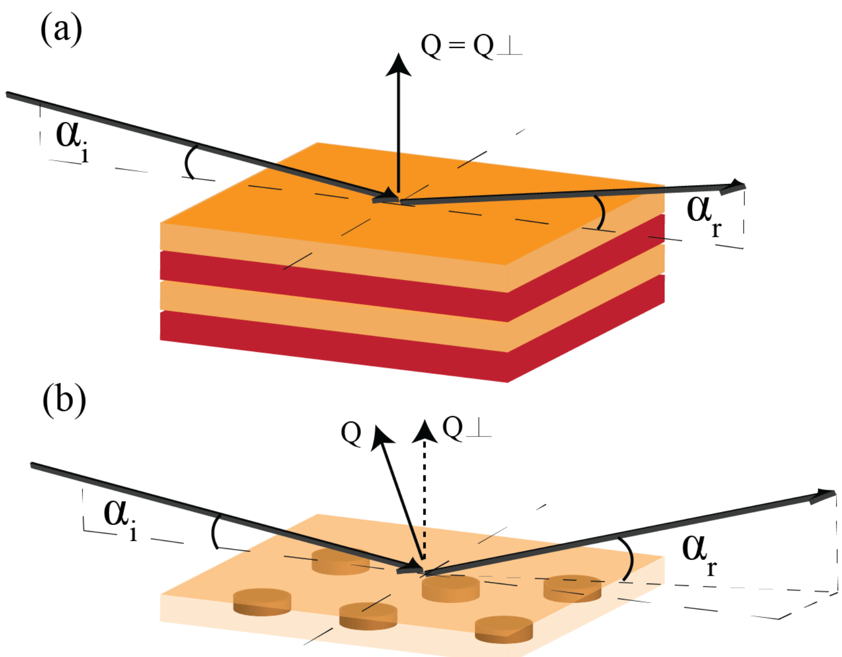

Figure 2.4: Diagram of Reflectometry configurations (a) Specular reflections from layered structure. The incident angle equals the reflected angle. (b) Off-specular reflections due to in-plane structure. Q is the momentum transfer vector.

encodes the depth-resolved average structure. From this technique, we can determine the thickness of layers within the sample and the sharpness of their interfaces (roughness). These layers may be distinguished by their nuclear scattering length density (SLD), SLD; the SLD encodes how strongly a material interacts with a neutron or magnetic SLD; the magnetic SLD encodes how strongly a magnetic material interacts with a neutron.

In reflectometry measurements, there are two main types of measurement. The first, and most common, is specular reflectometry in-which the incident angle is equal to the reflected angle, as measured relative to the sample surface, as shown in Fig. 2.4(a). This measurement configuration captures information planes within the sample parallel to the sample surface. Another measurement configuration is off-specular scattering in-which the incident angle (relative to the sample surface) is not equal to the exit angle (Fig. 2.4(b)) and occurs due to structure in the plane of the sample.

2.3 Polarized Neutron Reflectometry (PNR)

Since the neutron has a magnetic spin moment, it scatters from magnetic materials based on their relative alignment. In performing polarized neutron reflectometry (PNR) measurements, the spin of the neutron is polarized be 'up' or 'down'. During a reflectivity measurement, the neutrons experience the magnetization as an additional contribution to the scattering potential, depending on if the magnetization is parallel

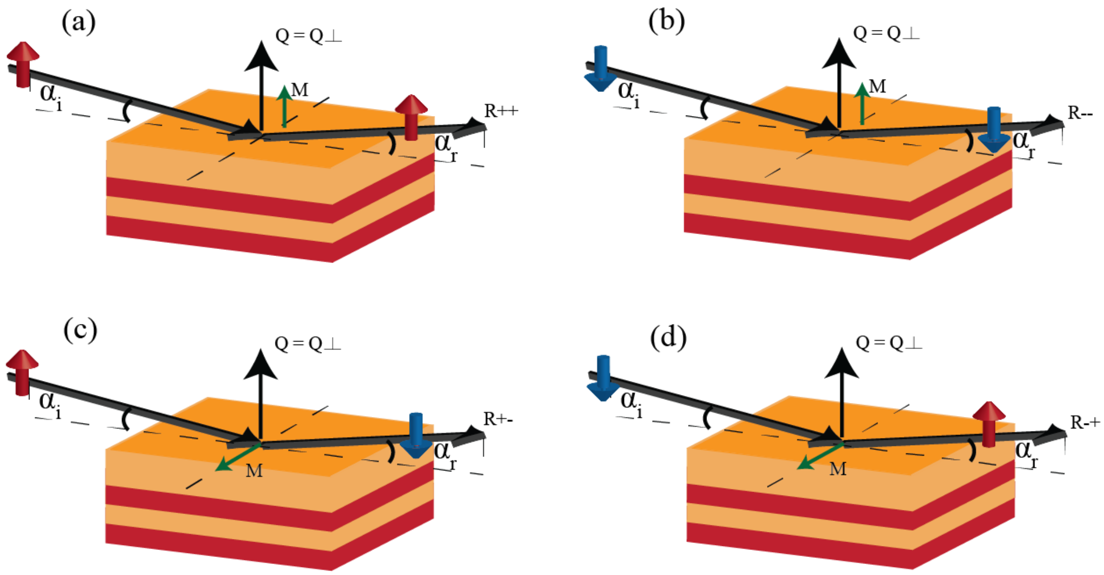

Figure 2.5: Four reflected cross sections spin (a) up-up (b) down-down (c) up-down (d) down-up

or antiparallel to the neutron spin moment. Alternatively, the magnetization can be orthogonal to the neutron spin, resulting in a torque which flips the neutron spin orientation. During PNR measurements, the spin of the neutron before and after scattering is captured, identified as the non-spin flip (R++ and R−−) and spin-flip (R+− and R−+) signals, where +/- correspond to the incident and reflected neutrons being spin up or down (Fig. 2.5). Using this insight, the magnetic structure can be extracted.

PNR is insensitive to magnetization within the sample which is parallel to the momentum transfer vector, Q. As a result of this neutron scattering selection rule and the measurement configuration, which has Q aligned at/near the surface normal direction, PNR results have no sensitivity to magnetization along the out-of-plane direction. Also, ideal specular PNR data does not include any information about the lateral (in-plane) distributions within the sample, instead capturing only the average nuclear and magnetic SLD at any particular depth within the sample [29]. However, it has been shown previously that, if the lateral scale of the underlying structure is larger than the neutron coherence length, some information can be captured within the PNR signal [30]. To analyze the data Refl1D software [31] is used. This software tool, developed at NIST, uses an iterative process to develop an SLD model and compare the calculated pattern from the model to the experimental results. This tools has been developed only for specular reflectometry.

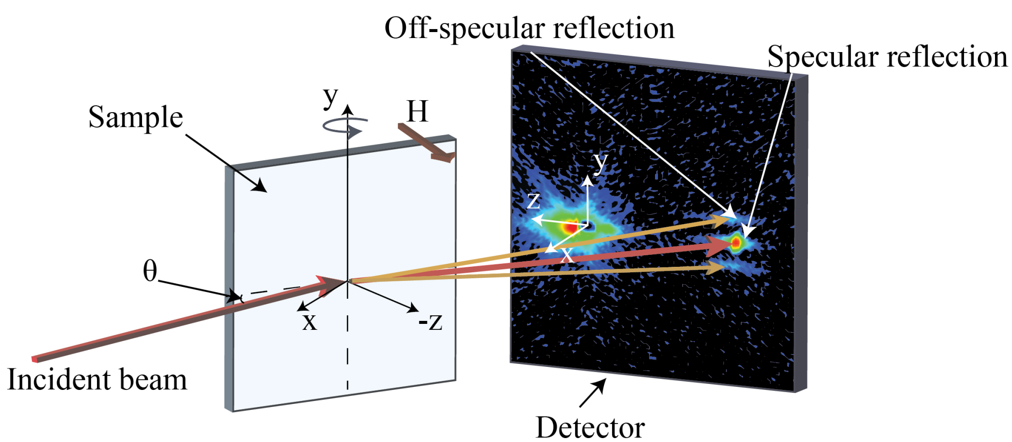

Figure 2.6: Schematic of the GISANS experiment setup. The diagram shows the sample illuminated at grazing incidence, with the specular (red arrow) and off-specular reflection (orange) scattering indicated.

2.4 GISANS

As the above section on neutron reflectometry explains, the specular configuration only provides the average SLD at each depth within the sample and so (nominally) has no sensitivity to any in-plane structure. Complementary to PNR, SANS provides only information about the in-plane structure averaged over the sample depth, e.g. with no sensitivity to the structure along the sample's depth. GISANS is a technique which combines these approaches, using a grazing-incidence configuration similar to PNR, but simultaneously capturing the off-specular scattering in the SANS detector, capturing both the in-plane and out-of-plane structure, as shown in Fig. 2.6. [32, 33]

2.5 Vibrating Sample Magnetometry (VSM)

Vibrating sample magnetometry (VSM) is an indirect measurement technique (measurements that indirectly probe the magnetism by e.g., probing the magnetic fields generated by the moments) and it is the most common method of measuring magnetometry. VSM measures the magnetic moment of the sample, therefore, the sample's magnetization. The basic mechanism of VSM is detecting the flux change in a set of coils when a magnetized sample vibrates near it. [34] The sample is mounted into a sample holder (made from quartz or brass) by using rubber cement (heptane and isopropanol) and inserted into the pickup coil set inside the sample chamber. Then the sample is driven back and forth through the pickup coil with the frequency of 40 Hz by using a linear motor. The oscillating sample inside the coil set generates

Figure 2.7: Dynacool PPMS at Gilbert lab

an alternating emf in the pickup coils, which is proportional to the magnetic moment of the whole sample. The Quantum Design PPMS (physical property measurement system) which we use, has the capability to generate a vertical magnetic field up to +/- 9 T. VSM also can be used in a wide range of temperatures with the range of 1.6 K to 400 K, and capable of resolving the magnetic moments $< 1 \times 10^{-6}$ emu. PPMS instrument situated in Gilbert Lab is shown in Fig. 2.7

2.6 Object-Oriented Micromagnetic Framework

Magnetic systems were modeled using a micromagnetic simulation software developed by NIST called the Object-Oriented Micromagnetic Framework (OOMMF) [35]. This software applies the Landau–Lifshitz–Gilbert (LLG) equation (2.3) and an energy minimization technique to model magnetic configurations and their response to magnetic fields.

$$\frac{d\bar{m}}{dt} = -\frac{\gamma_0}{1+\alpha^2}\bar{m} \times \bar{H}_{\text{eff}} - \frac{\gamma_0 \alpha}{1+\alpha^2}\bar{m} \times \left(\bar{m} \times \bar{H}_{\text{eff}}\right) \tag{2.3}$$

where $\bar{m}$ is the magnetization, t is time, $\bar{H}_{\text{eff}}$ is the total effective magnetic field, γ is gyromagnetic ratio and α is the damping constant. This program includes the magnetic energies, such as the exchange interaction, uni-axial anisotropy, magnetostatic energy, DMI and Zeeman energy. The equation for each of these terms is included in eq.2.4.

$$E = -A\bar{m} \cdot \nabla^2 \bar{m} - \frac{1}{2}\mu_0 M_\mathrm{s} \bar{m} \cdot \bar{H}_\mathrm{d} - \mu_0 M_\mathrm{s} \bar{m} \cdot \bar{H} - K(\bar{m} \cdot \bar{u})^2 + D\bar{m} \cdot (\nabla \times \bar{m}) \quad (2.4)$$

In above equation A, M_s, H_d, K, and D represents exchange stiffness, saturation magnetization, demagnetisation field, anisotropy constant, and dmi constant respectively. OOMMF software first discretizes the simulation volume into small finite-size cells. Each of these cells can be thought of as a single particle and considered homogeneously magnetized. When defining the cell size for the simulation, it is important to consider the magnetocrystalline exchange length (2.5) and magnetostatic exchange length (2.6) for a given set of parameters. The exchange length describes the lengthscale overwhich the exchange interaction dominates and the magnetic orientation is considered uniform. The simulation cell size must be smaller than the mentioned exchange lengths to prevent the dominance of exchange interactions in adjacent cells, which would obscure the observation of domain walls within different regions.

$$l_{ex} = \sqrt{\frac{A}{K_u}} \quad (2.5)$$

$$l_{ex,M_s} = \sqrt{\frac{2A}{\mu_0 M_s^2}} \quad (2.6)$$

The current version of OOMMF includes contributions from exchange and DMI, magnetocrystalline anisotropy, and dipolar interactions and allows periodic boundary conditions to micromagnetic simulations. The initial magnetic configurations with all the simulation parameters are first written into a single file called *miffile* and uploaded into the software using a command line or GUI-based application.

During the simulation, the software progresses step by step, employing an *evolver* that calculates the total energy of the system and derives the effective field based on this energy. The effective field is then applied to the Landau-Lifshitz-Gilbert (LLG) equation, changing the magnetization and, yielding a new effective field. This iterative process continues until a specified stopping condition is met.

2.7 Samples

My work has used both thin-film and bulk (B20-structured) sample materials. Thin-film multilayers of Ta(50 Å)/[(Fe (3.6 Å)/Gd (4.0 Å)]$_{120}$/Ta(50 Å) were grown on a 1 cm $\times$ 1 cm Si (001) substrate with a native oxide layer by DC magnetron sputtering, as described previously [3, 24]. The Ta was included as seed (adhesion) and capping layer to prevent the oxidizing (Fig. 2.8). The layered structure of the Gd/Fe induces a perpendicular magnetic anisotropy, e.g. the magnetic easy axis is along the film-normal direction. X-ray diffraction measurements show no apparent peaks, indicating the film is amorphous or nanocrystalline. For the bulk samples, single crystals of $Fe_{0.85}Co_{0.15}Si$ (FCS) and MnSi were grown by the Bridgman method in a floating zone furnace using previously published methods. [36, 37] Single crystals of Cu_2OSeO_3 were fabricated from CuO and SeO_2 precursors using solid state chemistry, also described previously [38].

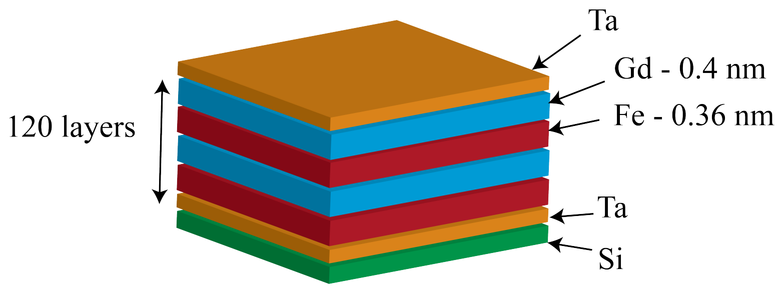

Figure 2.8: Fe-Gd ML system with Ta as capping and seed layer.

Chapter 3

Three-Dimensional Structure of Hybrid Magnetic Skyrmions Determined by Neutron Scattering

3.1 Introduction

The topology of magnetic skyrmions is a direct consequence of spin configuration, more generally described as the magnetic structure. In conventional, e.g. B20, skyrmions systems, the in-plane wrapping can be Néel-type, with the magnetic moments curling along the radial direction between the core and the perimeter, or Bloch-type, with the moment curling in the azimuthal direction, as described previously. [23] Recently, skyrmions which are stable across a wide range of temperatures and magnetic fields (10 K – 325 K; 30 mT – +200 mT) have been reported in Gd/Fe multilayers. [3] These skyrmions are proposed to have a hybrid structure consisting of both Bloch and Néel-type components.[39, 24, 40] The hybrid skyrmion can be considered in a thin film as a Bloch-type skyrmion with flux closure domains at the ends of the tube, i.e. where the skyrmion tube meets the top and bottom surfaces of the film; the flux closure domains are in-plane structures which act to vector the dipolar fields into the film, reducing the magnetostatic energy (Fig. 3.1). [41, 42] These flux-closure domains follow the contour of the skyrmion tube, themselves forming a closed wrapping, making them equivalent to a Néel-type skyrmion. Since the in-plane component of the dipolar fields are in opposite directions on the top and bottom surface, the flux-closure domains will have opposite chiralities. Thus, a hybrid skyrmion can be generally described as a three-dimensional stack of three skyrmions, evolving from Néel-type at one end of the skyrmion tube to Bloch-type, and back to Néel-type at the opposite end of the skyrmion tube, with the two ends having opposite chiralities. [3, 39, 24, 43] Also notable, while conventional skyrmions are stabilized by the Dzyaloshinskii-Moriya interaction, skyrmions in the Gd/Fe system are stabilized by dipolar interactions; since the flux-closure domains, e.g. Néel-type caps, also shape the dipolar fields, the stability, which has been demonstrated as exceptional, is directly related to the structure.

The three-dimensional structure of magnetic skyrmions is critical to their topology, stability, and their dynamic properties when perturbed with external forces. Verifying and quantifying their three-dimensional structure is important to understand these

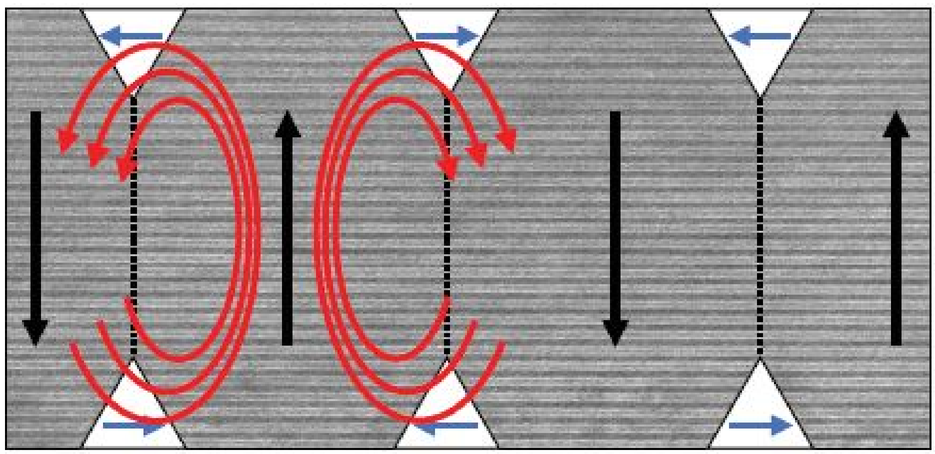

Figure 3.1: Schematic of flux closure domains. Red lines represent magnetic field lines, and blue arrows represent Néel caps in the sample. [3]
Bright and dark lines represents Fe/Gd multi layers

features. Previous works have used electron holography to determine the three-dimensional structure of conventional Bloch-type magnetic skyrmions in nanowires, at dimensions limited by the transmission of electrons through the material. [44] For hybrid skyrmions in particular, the requirement that there is a significant dipolar interaction and uniaxial anisotropy means these features preferentially manifest in thin films and would likely be unstable in nanowires. To better understand the stability of hybrid skyrmions, it is critical to determine their three-dimensional structure in thin films.

Addressing the need for an *in-situ* probe of the hybrid skyrmion structure requires a penetrative, non-destructive tool such as neutron scattering, [45, 46] which has been used extensively in skyrmion research due to its sensitivity to nanoscale magnetic features. However, the vast majority of these investigations have been performed on bulk materials due to limitations in signal strength and lack of skyrmion thin-films with long-range coherent order.[47] Hybrid skyrmions observed in Fe/Gd multilayer thin-films have been previously measured with transmission SANS, which captures the in-plane hexagonal ordering of the skyrmion lattice but not its depth profile.[3] Alternatively, polarized neutron reflectometry (PNR), which is typically performed in a specular reflection geometry, provides access to the structural and magnetic depth profile, but only the depth-resolved average; in-plane structure is generally not probed with specular PNR.[48] By combining these techniques in an appropriate scattering geometry, grazing-incidence small-angle neutron scattering

(GISANS) and off-specular PNR allow simultaneous access to the in-plane and out-of-plane structures. [33, 32, 49]

In this project, we perform PNR, SANS, and GISANS measurements to determine the three-dimensional structure of hybrid skyrmions in Fe/Gd multilayers.[3] First, SANS and PNR measurements are performed on a single thin-film to determine the structure of the film hybrid skyrmion latice. Next, GISANS measurements were taken. The results from the PNR and SANS experiments are then used to inform and constrain a micromagnetic simulation. Using a Born approximation algorithm, the GISANS patten from the simulation is calculated and compared to experimental GISANS data. Through iterative feedback between the experimental and simulated results, the micromagnetic simulation is adjusted to reproduce the experimental results. Our combined experiments and micromagnetic model reveal the complex three-dimensional structure of the hybrid skyrmion in a thin film magnet.

3.2 Experimental Procedure

Polarized neutron reflectometry measurements were performed using 5 Å wavelength neutrons, at room temperature, on the MAGIK reflectometer at the NIST Center for Neutron Research (NCNR). Measurements were performed in the saturated state with a 500 mT in-plane field, and in the skyrmion state with a small ($\approx$ 1 mT) out-of-plane guide field. By the scattering selection rules, the reflectivity is sensitive only to the projection of the magnetization in the sample plane that is perpendicular to the scattering wavevector, Q. [50] The saturated state provides magnetic and nuclear information in the non-spin flip channel (R++, R−−, where ++ (−−) indicates the incident and scattered neutron spin orientation as up-up (down-down), respectively). Specifically, the splitting between the R++ and R−− reflectivities in this scattering configuration originates in the projection of the net in-plane magnetization that is parallel to the applied field. In contrast, the out-of-plane guide field for the skyrmion state causes the magnetic information to manifest only in the spin-flip channel, R+− and R−+ (where +− (−+) indicated the incident and reflected neutron spin orientation as up-down (down-up)) [51], and R++ and R−− have contributions only from the structural scattering. Data fitting was performed using the Refl1d software package [52]; the models for the two field conditions were fitted in parallel, with the nuclear parameters coupled. The specular PNR technique is sensitive to the depth-resolved, average, in-plane magnetization, and is insensitive to in-plane magnetic regularity or out-of-plane magnetization.[48, 32]

SANS and GISANS measurements were performed on the very small-angle neutron scattering (vSANS) instrument at the NIST Center for Neutron Research using 14 Å neutrons at room temperature. The SANS measurements were performed with the neutron beam parallel to the film's out-of-plane direction and near-zero magnetic field, resulting in the diffraction pattern for the stripe (Fig. 3.2a) and skyrmion states (Fig. 3.2b). Grazing-incidence SANS measurements were performed by illuminating the sample at grazing incidence, similar to PNR but now on a SANS instrument. The incident angle was varied, between 0.3° to 0.9° in steps of 0.05°. An illustrative diagram of the GISANS measurement setup is shown in Fig. 2.6. Unlike PNR, GISANS captures the specular reflection, as well as any off-specular reflections from in-plane ordering. A small magnetic field is applied in the film's out-of-plane direction during the measurement. The sample was measured in the stripe, skyrmion and saturated states. Data are presented in terms of the momentum transfer vector, with Q_z defined as the out-of-plane direction.

Micromagnetic simulations were performed using the Object Oriented Micro Magnetic Framework (OOMMF) simulation platform. [35] This platform uses a macrospin approximation with cells 5 nm in the x and y direction and 1 nm in the z-direction; this length is smaller than the calculated exchange length. The total simulation area was 880 nm $\times$ 760 nm nm in the x and y directions, respectively, with a thickness in z-direction based on the PNR-determined depth profile. Magnetostatic, magnetocrystalline, and exchange energies are considered in the model with periodic boundary conditions, and no net DMI is expected in the experimental system. The anisotropy constant is determined from magnetometry using the in-plane saturation field and ferromagnetic resonance studies, and the saturation magnetization is determined using the experimental PNR results, measured at saturation (500 mT in-plane field). The simulations were allowed to relax to a steady state with zero applied magnetic field. Using the Born approximation and an in-house python code, the diffraction pattern is calculated from the OOMMF simulation for any scattering plane and neutron spin orientation. [48]

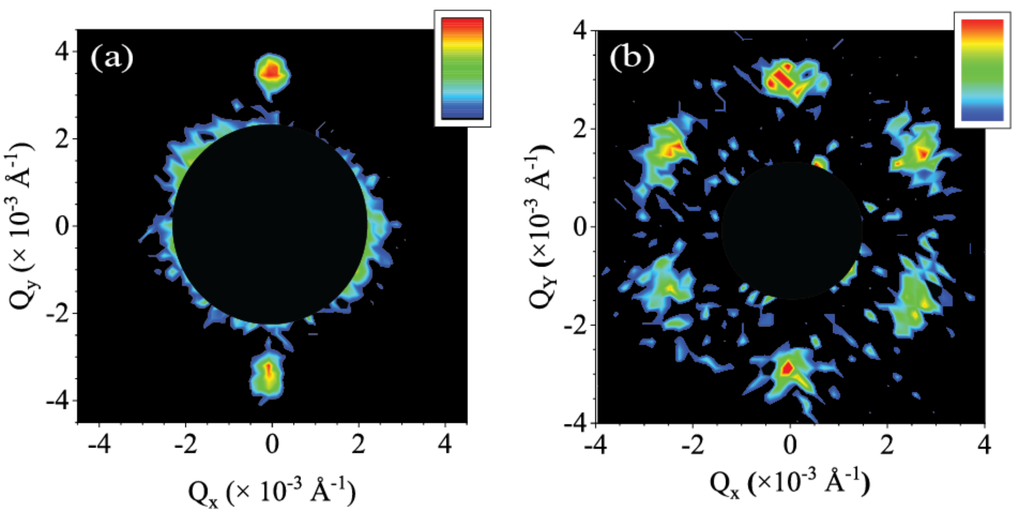

Figure 3.2: (a) Measured stripe state data for Fe/Gd ML showing two diffraction peaks. (b) Measured SANS pattern for the skyrmion state.

3.2.1 Results

SANS measurements were performed on single films of Fe/Gd multilayers in the stripe and skyrmion states. The SANS pattern measured in the stripe phase, Fig. 3.2a, shows two peaks located at $|Q| = \pm 0.00339$ Å^{-1}, corresponding to a real-space periodicity of 185 nm. The presence of only two peaks indicates that the stripes have a long-range orientation, as opposed to labyrinth domains which would show a uniform intensity ring-like SANS pattern [53]. The position of the peaks confirm that the long axes of the stripes are parallel to the direction of the in-plane field component during the preparation of the initial state. Subsequently preparing the sample in the skyrmion state, the SANS pattern has a six-peak hexagonal structure shown in Fig. 3.2b, representing the Fourier transform of the hexagonally-ordered skyrmion lattice within the film. As in the stripe phase, the hexagonal pattern in the skyrmion state demonstrates that the skyrmions are arranged in a well-ordered lattice which is highly oriented across the film plane. The peaks in the hexagonal pattern at zero field and room temperature are evident at $|Q| = 0.00298$ Å^{-1}, corresponding to a skyrmion center-to-center spacing of 211 nm. These data provide insight into the in-plane spatial ordering of the film, but do not provide details pertaining to the depth-dependent structure of the hybrid skyrmions through the film.

Complementary to the SANS measurements, PNR measurements provide details about the depth-resolved average structure. Neutron reflectometry results and the converged depth profile from the saturated and skyrmion state measurements are shown in Figs. 3.3(a, b) and 3.3(c, d), respectively. Since signal-to-noise limitations obscure the superlattice diffraction peaks from the [(Fe (3.6 Å)/Gd (4.0 Å)]$_{120}$ bilayers in these measurements, the multilayer structure is treated as a single composite Fe_xGd_{1-x} layer with a nominal x=0.47. The converged depth profile confirms the structure of the film to be Si / Ta(6.4 nm) / FeGd(81.7 nm) / Ta(5.3 nm) / TaO_x(2.2 nm) and provides an experimental nuclear scattering length density, (SLD), ρ_N) ρ_N(Ta) = 4.13×10^{-6} Å^{-2}, ρ_N(GdFe) = 3.76×10^{-6} Å^{-2}. These values are slightly different from the expected values for the bulk constituents (ρ_N(Ta) = 3.83×10^{-6} Å^{-2}, and ρ_N(GdFe) = 4.23×10^{-6} Å^{-2}) likely indicating some oxidation of the Ta and that the Gd layer thickness may be less than the nominal value. The Gd/Fe ratio uniquely identified by the imaginary SLD, ρ_{Img}, and corresponds to neutrons being absorbed by the film, which occurs exclusively in the Gd; no apparent critical edge is observed in the reflectometry due to the absorbing nature of the Gd.

The PNR data measured in the saturated state are shown in Fig. 3.3a, with the converged profile in Fig. 3.3b; the reflectivity from the model is shown as a solid line in Fig. 3.3a. The profile provides a magnetic SLD (ρ_M) which confirms that only the FeGd layer is magnetic, and it is uniformly magnetic throughout the entire thickness of the thin-film, with ρ_M(FeGd) = 0.99×10^{-6} Å^{-2}. The magnetic SLD can be transformed to a magnetization of 351 kA m^{-1} (1 kA m^{-1} = 1 emu/cm^3). Since Gd and Fe have an antiferromagnetic exchange interaction, this is the net magnetization from the antiparallel layers, as the applied magnetic field is insufficient to break the

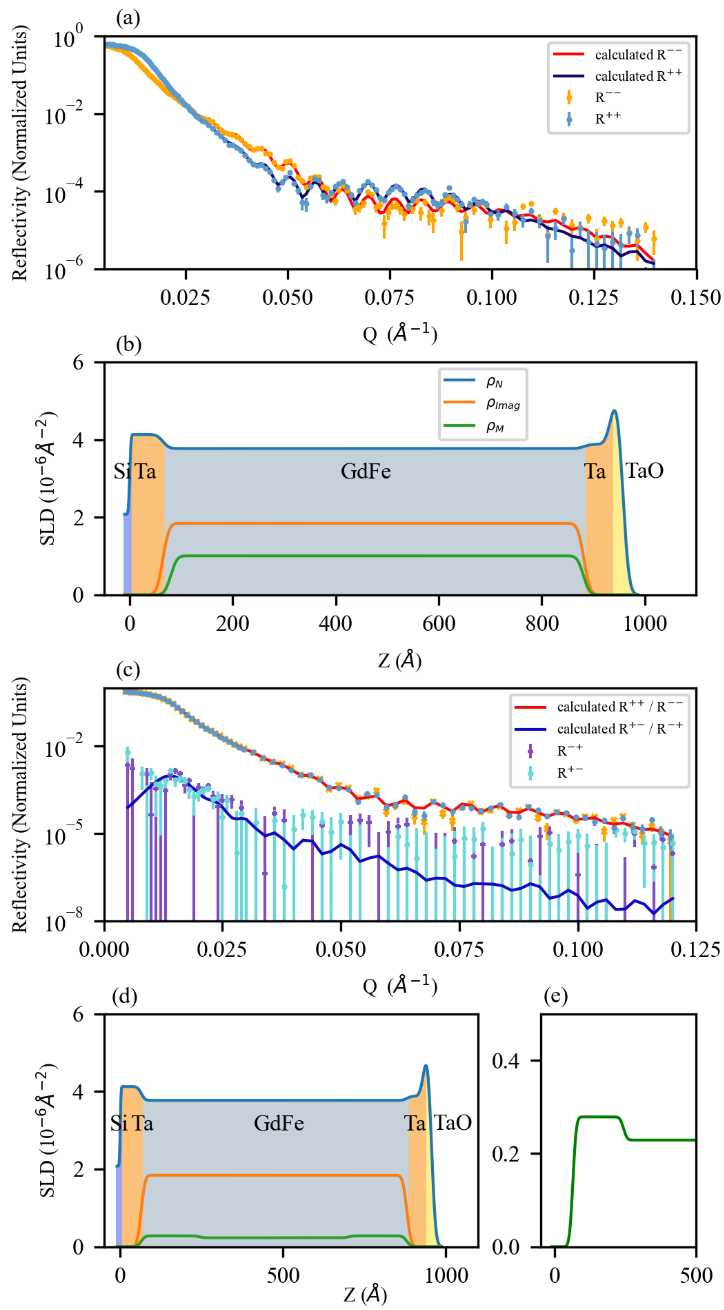

Figure 3.3: (a) Specular reflectivity measurement and (b) converged depth profile for the Gd/Fe multilayer in the saturated state (in-plane saturation, 500 mT). The neutron polarization axis is in-plane and parallel to the saturating field in this scattering configuration. Only the non-spin-flip data are shown since there is no appreciable spinflip signal in saturation. (c) Specular reflectometry and (d) converged depth profile measured in a 1-mT field, in the skyrmion state with the magnetic surface state emphasized in (e). For (a), the neutron polarization axis is in the plane of the film, while for (c), the neutron polarization axis is out-of-plane and parallel to the small guide field.

antiparallel coupling. [54] The saturation magnetization and structural parameters are used later to inform and constrain the micromagnetic simulations.

Reflectometry data taken in the skyrmion state are shown in Fig. 3.3c, with the fitted magnetic depth profile shown in Fig. 3.3d. The converged model shows a small in-plane magnetization through the middle of the film, with a slightly larger (≈20%) magnetization at the top and bottom surfaces. While an initial consideration of the PNR profile of a skyrmion would suggest that there should be no magnetic scattering, since the average in-plane magnetization for a skyrmion is zero, previous result have shown that this assumption is not correct.[48] Specifically, in PNR the neutron wave packet is reflected off the surface of the sample at a shallow angle, experiencing the average scattering potential from the sample within a volume defined by the longitudinal (i.e. at the intersection of the scattering and sample planes) and transverse (i.e. in the sample plane but perpendicular to the scattering plane) neutron coherence length. The longitudinal neutron coherence length in the reflectometers at NIST has been measured to be ≈100 μm, however the transverse coherence length is <1 μm. [30] If the transverse coherence length is not an integer multiple of the skyrmion periodicity, the neutron will interact with a non-integer number of skyrmions, i.e. catching the edge of a skyrmion. This extra part of the skyrmion within the neutron coherence length contributes a net in-plane magnetization. [48] Since an out-of-plane guide field is used, the orientation of these fractional skyrmions is irrelevant: they are all orthogonal to the neutron spin and contribute similarly to the spin-flip signal. This is important because it means that opposite edges of the skyrmion and their winding (Bloch or Néel) all contribute to the average. As a result, the PNR spin-flip signal is non-zero and possesses a sensitivity to the in-plane magnetization. Similar discussions were presented previously in Ref. [48]. Based on this understanding, peaks in the magnetization near the top and bottom of the GdFe layer in the skyrmion state, shown in Fig. 3.3d, suggest that the Néel caps have a larger in-plane footprint than the Bloch-type wrapping around the equatorial band. The thickness of the top and bottom magnetization peaks provides the first insight into the thickness of the Néel caps, which we can identify here as approximately 17.9 nm (1σ confidence interval of 11.9 nm – 18.4 nm).

GISANS

Grazing-incidence SANS, similar to off-specular reflectometry, provides simultaneous insight into the in-plane and out-of-plane structure. As noted above, GISANS measurements were taken at a series of angles (θ) between 0.3° to 0.9° in steps of 0.05°; where θ corresponds to the angle between the sample and the neutron beam (Fig. 2.6). At each angle, the 2D scattering pattern was captured, as shown in Fig. 3.4a for $\theta = 0.5°$ in the stripe phase. In this state, three GISANS peaks can be observed, one at finite Q_z and $Q_y = 0$, representing the specular reflection, and two at $Q_y = \pm 0.00338$ Å^{-1}, representing the off-specular diffraction. The peak location along the Q_z coordinate corresponds to the traditional 2θ position in standard reflectometry or diffraction geometry and changes with the sample angle. The peak location along

Q_y is determined by the in-plane periodicity, which for the stripe phase is 186 nm. The stripe state corresponding to zero applied field has two peaks analogous to the transmission SANS pattern shown in Fig. 3.2a.

Compared to the stripe domain configuration, the specular scattering in the skyrmion state is nearly identical while the off-specular scattering intensity is much weaker and has a narrower distribution along the Q_z direction, as shown in Fig. 3.4b. The off-specular peaks can be observed at Q_y = 0.0025 $Å^{-1}$ when measured in a magnetic field μ_0H = 190 mT, corresponding to a real space periodicity of 251 nm. Our previous work [3] showed that in these hybrid skyrmions, the periodicity increased at larger fields following a soliton lattice theory. [55] To further clarify that these peaks are solely from the magnetic structure, GISANS measurements were performed in the saturated state using an out-of-plane magnetic field. The external field pulls the magnetic moments in the z direction (out-of-plane direction). According to the neutron selection rules, the contribution to the magnetic scattering at the specular position should be zero if the sample is saturated. The magnetic peaks at finite Q_y should be evident if the skyrmion lattice persists. Instead, these peaks are gone, which indicates off-specular peaks originated from the regular in-plane magnetic structure, as shown in Fig. 3.4c. We may therefore reliably conclude that the off-specular scattering is exclusively magnetic in nature.

Preliminary analysis of the data can be performed by reducing the specular data from the GISANS measurements to a 1D intensity versus Q_z plot and comparing this with the PNR results. As noted above, the specular reflection in the saturated

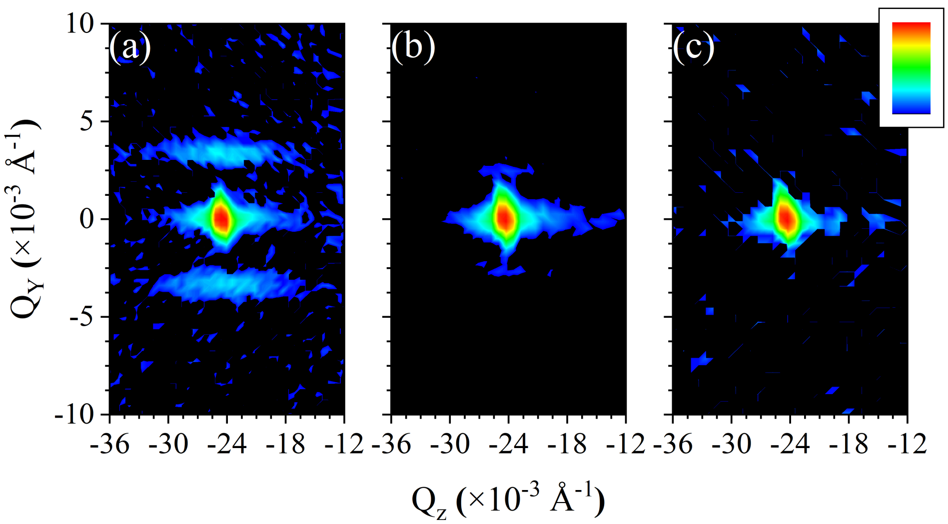

Figure 3.4: Grazing-incidence small-angle neutron scattering (GISANS) data in (a) the stripe state, (b) skyrmion state, and (c) saturated state. The z contrast uses a logarithmic scale. For all three measurements, the specular peak appears at $Q_y = 0$, while the off-specular peaks appear at $Q_y = \pm 0.00338$ Å^{-1} and ± 0.0025 Å^{-1} for the stripe and skyrmion states, respectively.

state, measured with an out-of-plane guide field, captures the nuclear structure, which was also measured in the PNR measurements (R++ and R−− in Fig. 3.3c). The converged nuclear depth profile from Fig. 3.3d is used, with ρ_M set to zero, to generate the corresponding nuclear-only reflectometry with GISANS instrumental conditions; this reflectometry pattern is compared to the 1D GISANS results in Fig. 3.5 and shown to agree well, with a chi-squared (χ^2) of 1.21. Alternative models were tested and produced poorer fits, with a 'flat' magnetic structure resulting in a χ^2 of 2.87 and a non-magnetic structure 2.07. To analyze the off-specular peaks, a physics-based model of the magnetization is generated using the OOMMF simulation platform; the GISANS pattern from the OOMMF result is calculated and compared to the experimental results. [33]

The intensity of the off-specular peaks is integrated along Q_y and used to generate a 1D plot of the of the off-specular intensity as a function of Q_z, shown in Figure 3.6. Since this off-specular scattering appears at finite values of Q_z and Q_y, these data encode both the in-plane and out-of-plane structure, respectively, of the hybrid skyrmions. The next section discusses the micromagnetic model used to generate the simulated data in Figure 3.6.

Micromagnetic modeling

Hybrid skyrmions were simulated using physical parameters derived from the experimental results. The saturation magnetization was determined from magnetization measurements to be 351 kA m^{-1}; the uniaxial anisotropy constant (K_u) was

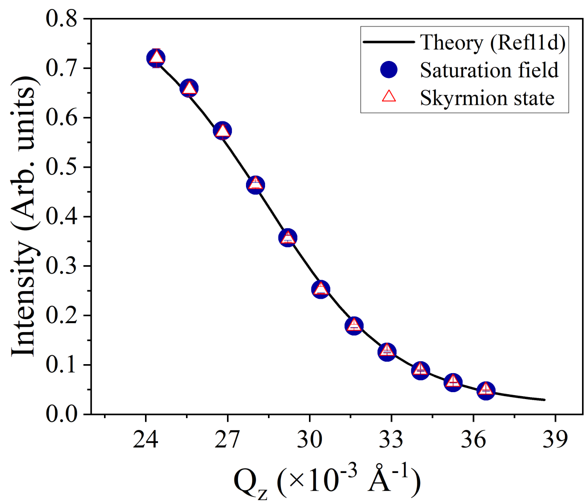

Figure 3.5: Integrated intensity of the specular reflection from GISANS for the skyrmion (triangle), out-of-plane saturated states (circle), and theory from the Refl1d model (line)

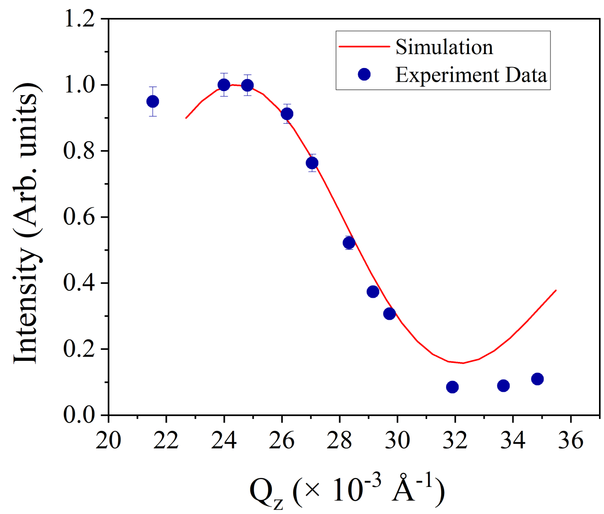

Figure 3.6: Integrated intensity from the off-specular diffraction peak from GISANS (circle) and theoretical results from micromagnetic modeling (line).

determined to be 1.8×10^5 J m^{-3} using the in-plane (hard-axis) saturation field.[56] The lateral exchange stiffness (A) was adjusted to achieve a stable skyrmion configuration with a periodicity that matched the experimental SANS results, converging to a value of 0.7×10^{-11} J m^{-1}. This parameter is expected to be much less than iron (2.1×10^{-11} J m^{-1}) [57] due to the nearly 2D nature of the film layers and was the primary control variable in the modeling. For reference, this value is slightly less than nickel (0.9×10^{-11} J m^{-1}) and is consistent with ferromagnetic resonance measurement in Ref. [24]. The vertical exchange stiffness was fixed at 10% of the lateral, reflecting the difference between Fe-Fe exchange coupling and Fe-Gd exchange coupling.[54] The initial state of the system was prepared with hybrid skyrmions, which has Néel caps at the ends of the skyrmion tube and a Bloch-type winding at/near the equatorial band. Then the micromagnetic simulation was allowed to relax in zero field. For the case of too large or small A, K_u or M_s, the state collapsed to labyrinth domains or a saturated state. Including a DMI term results in ejection of the Néel-type surface states, resulting in traditional Bloch-type tubular skyrmions. The model was also tested by starting with only Bloch or Néel-type states, or Néel-type (flux closure caps) with the same chirality, all of which relaxed to the hybrid configuration or collapsed to a saturated or labyrinth state, confirming the robustness of the hybrid skyrmion configuration. The simulation space (880 nm $\times$ 760 nm $\times$ t, where t is the layer thicknesses determined from PNR) captures an array of 16 skyrmions.

A plane view image and a series of real-space slices of a single hybrid skyrmion from the converged model are shown in Fig. 3.7(a-f). This simulation, which includes all of the underlying physics of the magnetic interactions, confirms the proposed structure, including the Néel-type surface states with opposite chirality at the top and bottom portion of the thin-film, and a Bloch-type winding at/near the equatorial band. Comparing Figs. 3.7b and 3.7f with 3.7c-e, we see that the width of the skyrmion boundary is larger in the Néel caps (b and f) and narrower in the Bloch region (c-e). The in-plane width of the skyrmion boundary is extracted by fitting a Gaussian function to the in-plane magnetization and determining the width, and is plotted in Fig. 3.8a. The width of the boundary is shown to increase from 16 nm at the equatorial band to 22 nm in the Néel caps. Since the in-plane magnetization detected by PNR originates within this in-plane boundary region, a larger skyrmion boundary width yields a larger effective in-plane magnetization in PNR. To understand this scaling, Fig. 3.8b plots the total in-plane magnetization at each depth ($1 - \int |M_z| dxdy$) alongside the magnetic SLD from the PNR results. We note that while the spin-flip PNR is sensitive to the in-plane magnetization averaged over the neutron coherence length rather than the total in-plane magnetization as defined above, the two signals are expected to be approximately linearly related to each other in this case. As discussed above, the magnetic SLD detected by PNR in this system is governed by the coherence volume of the neutron wave packet, which overlaps with a non-integer number of skyrmion boundaries such that a residual in-plane magnetization is detected.

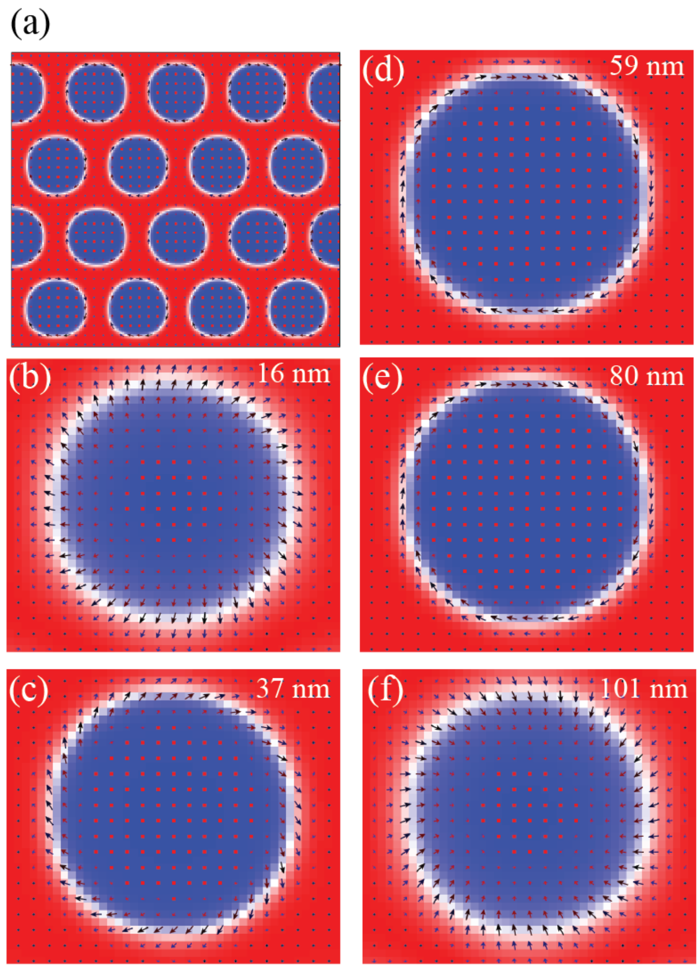

Figure 3.7: (a) Plane view image of the simulated skyrmion lattice. (b)-(f) Slices of the magnetic configuration taken along the length of the skyrmion tube, with (b) Z=16 nm corresponding to the top surface and an inward wrapping Néel cap, (d) Z=59 nm corresponding to the middle and a clockwise Bloch type, and (f) Z=101 nm corresponding to the bottom surface and an outward wrapping Néel cap.

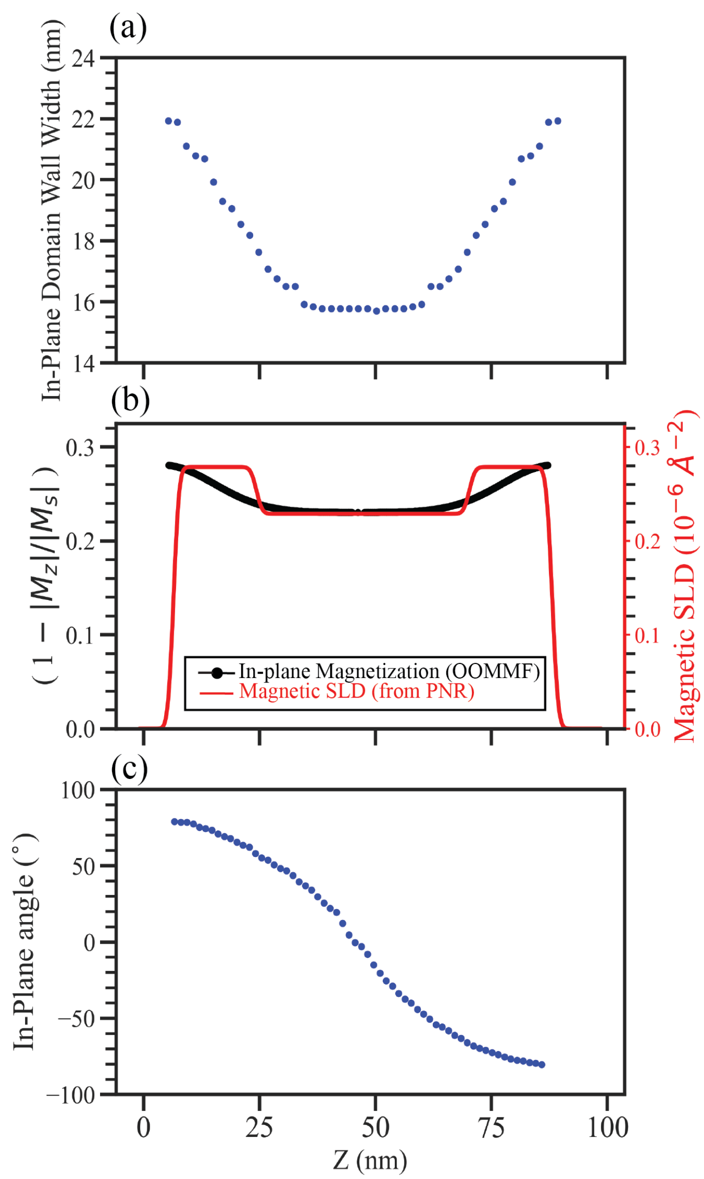

Figure 3.8: (a) The in-plane width of the skyrmion boundary region. (b) The total in-plane magnetization from OOMMF integrated versus depth and compared to the magnetic SLD profile from the PNR results. (c) The in-plane angle of the skyrmion boundary region versus depth, with +90°/0/-90° corresponding to inward Néel, clockwise Bloch, and outward Néel, respectively. Note that 0○ is defined as the azimuthal direction.

Comparing the OOMMF model to the Refl1D model, the structures are very comparable. The nuclear structures are nearly identical by design and are thus not shown. The magnetic profiles of both models similarly show a larger magnetic feature near the surface. The thickness of the feature is 13 nm in the OOMMF model and 17.9 nm (1σ confidence interval of 11.9 nm $-$ 18.4 nm) in the Refl1D model. Notably, the OOMMF model is within the confidence interval of the experimental data. The key difference in the two magnetic profiles is the sharpness of this feature, more specifically the interface between the Bloch and Néel regions. The OOMMF model shows a wide boundary, spanning nearly 30 nm, while the Refl1D model has a much sharper interface of 4.3 nm $\pm$ 2.3 nm. The Refl1D model has poor sensitivity to this feature since the large width of this magnetic interface will generate exceedingly weak reflectometry fringes for larger interface widths.

Another interesting insight provided by the OOMMF results is the continuous evolution of the Néel/Bloch/Néel structure with depth. Specifically, Figures 3.7(b) and (f), which correspond to the ends of the skyrmion tube and should be Néel-type, are not entirely oriented along the radial direction in the boundary region. Instead they are canted by an average of 13° towards the azimuthal direction. Figures 3.7c and 3.7e, which are between the Bloch and Néel regions, show that the spin moments are oriented between the radial and azimuthal directions. The equatorial band of the skyrmion tube, Figure 3.7d, is oriented along the azimuthal direction, and is therefore a proper Bloch structure. The angle of the magnetic moment in the boundary region versus depth is extracted and plotted in Figure 3.8c. This plot shows that the angle of the spins, relative to the azimuthal (in-plane) direction, changes continuously throughout the film. While PNR is sensitive to the width of the boundary region with in-plane spins, the angular orientation of the moments within the plane cannot be distinguished in our scattering geometry. Interestingly, while the skyrmion boundary width has three distinct regions, which we above identify as the surface Néel caps and the Bloch region, the spin angle, which is the actual identifier of the Néel and Bloch regions, e.g. the in-plane angle of the magnetization in the boundary, is more continuous.

Using a Born approximation-based Python code, the PNR, SANS, and GISANS diffraction patterns from this structure were generated from the converged micromagnetic profile. The code included the real and imaginary nuclear structure as determined by PNR, and the magnetic structure determined by the micromagnetic model, constrained by the PNR-determined nuclear structure and magnetization. The roughness between each layer in the modeled system (e.g., Si/Ta, Ta/GdFe, GdFe/Ta, Ta/TaO, TaO/air) was coarsely treated as a 1 nm thick boundary layer with an SLD defined as the average of the adjacent layers; this limitation is set by the cell size in the micromagnetic model. Also included in the code was the spin of the neutron, defined to be along the film normal direction, matching the experimental measurements, and in the scattering plane. For comparison to the data in Fig. 3.2b, a preliminary simulation in the SANS (transmission) geometry was calculated and is shown in Fig. 3.9. The structure confirms the hexagonal pattern which also appears in the simulated structure. Additional peaks and stretching along the Qy direction

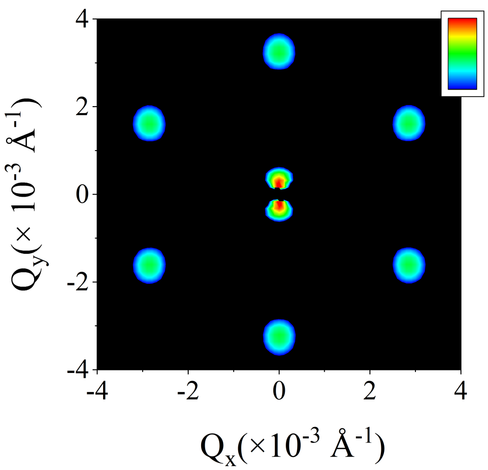

Figure 3.9: Calculated 2D transmission SANS from simulation

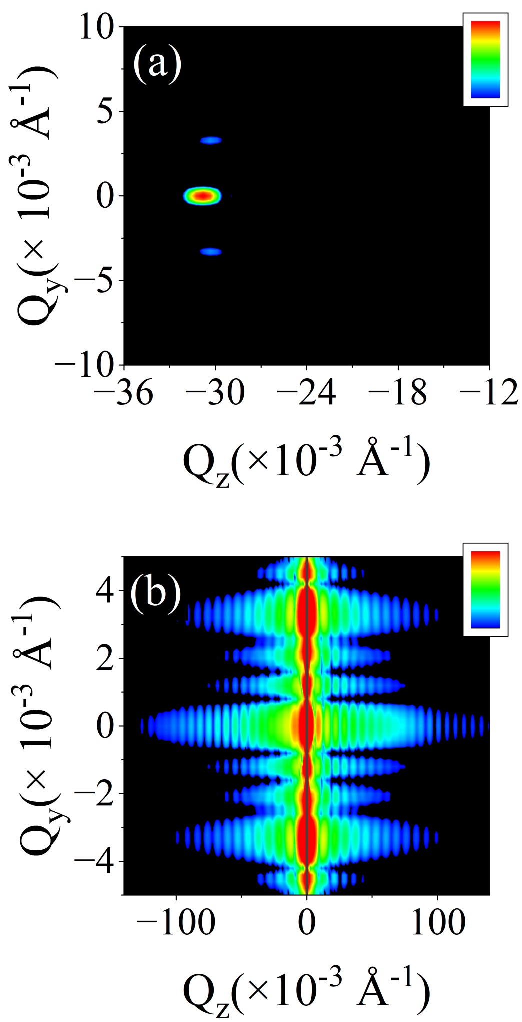

Figure 3.10: (a) grazing-incidence SANS(GISANS) measurements simulated at $Q_z = -0.031$ Å^{-1} (b) cumulative GISANS pattern from the OOMMF simulations of the skyrmion state. The z-contrast uses a logarithmic scale. The cumulative GISANS pattern is the sum of all measured theta angles (i.e., all measured Q_z values), while the experimental results are measured at sequential angles, analogous to panel (a) and Fig. 3.4b.

are the result of the finite volume of the simulation and fractional skyrmions on the boundary of the simulation space. The calculated diffraction peaks appear at $|Q| = 0.0033$ Å^{-1}, consistent with the experimental results, which showed $|Q| = 0.00298$ Å^{-1}, confirming the simulation captures the mesoscopic structure.

Next, the GISANS pattern, for this structure was calculated along the Q_y and Q_z directions, as shown in Fig. 3.10a. The simulated result is calculated at a single reflection angle to emulate the experimental result, and indeed generates a similar structure to Fig. 3.10a. The reflectometry data – which is operationally identical to a GISANS measurement captured at Q_y=0 – and GISANS data were measured at a series of sample angles then integrated to establish curves versus Q_z; an integrated series of GISANS measurements is shown in Fig. 3.10b. Both at the specular reflectometry (Q_y=0) and off-specular position (Q_y=0.0033 Å^{-1}) the Kiessig fringes are clearly visible, indicating a sensitivity to the depth profile. From these data, all four scattering cross-sections (R++, R−−, R−+, R+−) are extracted at $Q_y = 0$ and $Q_z < 0$ (corresponding to a front-side reflection), generating a model of the specular reflectometry pattern based on the OOMMF model which is comparable to the experimental data and Refl1D fit in Fig. 3.3c. The experimental, Refl1D and OOMMF models are compared in Fig. 3.11. The non-spin flip signal reproduces all of the major features and structure in both the Refl1D and OOMMF models, which is expected because it is based on only the nuclear structure, which is programmed to be nearly identical. The spin-flip data are comparable, with a notable matching of the higher frequency oscillations. Notable differences in the spin-flip signal can be seen by a more rapid decay in the Refl1D model and a damping of the high-frequency oscillations at Q_z=0.075 Å^{-1}. The former feature is likely a result of the background subtraction, and a limited ability to model roughness in the OOMMF model. The latter feature is likely a consequence of the small surface domains having a much sharper interface in the Refl1D model (converged to be 4.3 nm ± 2.3 nm) compared to the OOMMF model, which changes continuously over nearly 30 nm. The Refl1D has poor sensitivity to this feature since the large width of this magnetic interface will generate exceedingly weak reflectometry fringes.

The off-specular features from the GISANS data are also calculated and compared to the experimental results in Fig. 3.6; these calculated data are the sum of the R++, R−−, R+−, and R−+ to reproduce the experimental results. Compared to the PNR range, the GISANS range is limited because the detector must be located at the maximal distance in the SANS tube and measured with a long neutron wavelength to separate the off-specular signal from the specular reflection. However, in this configuration only a very small range of sample angles can be measured before the beam is off the edge of the detector. Nevertheless, the calculated results accurately reproduce the experimental data in Fig. 3.6e. Furthermore, these data capture the critical fall-off region in-which the neutrons penetrate the sample and interact strongly, and also present maximal neutron fluence and maximal statistical importance.

Together the OOMMF and Refl1D models are complementary. Both propose to determine the structure of the skyrmion, with the Refl1D approach utilizing scattering

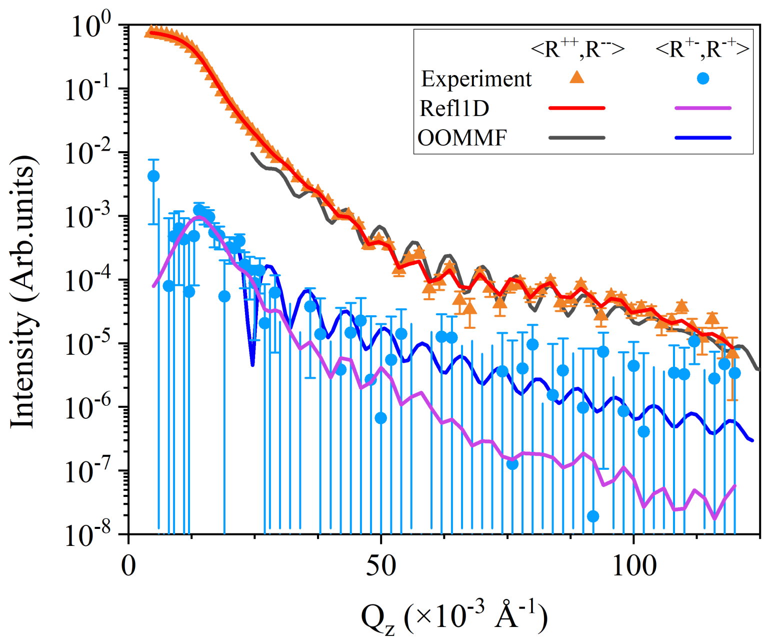

Figure 3.11: Average non-spin-flip specular reflectivity <R++,R−−> and spin-flip reflectivity <R+−,R−+> from PNR, OOMMF (1D depth profile) and three-dimensional micromagnetic simulation (OOMMF, shown in Fig. 3.7) at $Q_y = 0$. A constant background was added to the three-dimensional OOMMF model.

with no consideration for the underlying magnetic energies, while OOMMF has no ability to experimentally confirm its predicted structure but includes these magnetic interactions. This work has shown that the Refl1D model accurately captures key features of the system, such as the thickness of the surface state, but misses others, such as the interface width of this feature. OOMMF also provides insights which cannot be captured by scattering, such as the rotation angle of the in-plane moments, or their correlation with the surface states. Together, these results provide a structure that is grounded both in fundamental physics and confirmed through experimental investigation.

Discussion

Hybrid skyrmions have been demonstrated as one of the few chiral magnetic systems which are stable at room temperature and zero magnetic field, making them a strong candidate for skyrmion-based technologies. Their exceptional stability can be attributed to their hybrid structure, specifically the flux-closure domains on the ends of the skyrmion tubes, that decrease the magnetostatic energies in the system. The structure is also key to the topology of the system and its dynamic response for high frequency applications. The present work experimentally determined the three-dimensional structure of the hybrid skyrmion using a combination of neutron scattering techniques and physics-based modeling. Using PNR and SANS, the in-plane and depth-averaged magnetic structure is determined. Details from these measurements are used to inform and constrain a physics-based micromagnetic model, which was iteratively improved to reproduce the experimental results. The micromagnetic model was subsequently verified by comparing with grazing incidence SANS results, which simultaneously captures the in-plane and out-of-plane structure. The real-space spin structure, provided by the micromagnetic model, first verifies the three-dimensional construction of the hybrid skyrmion and provides new insights about their structure. Key among these features is that the thickness of the Néel caps (13 nm – 18 nm), the continuous winding of the in-plane angle, and the changing width of the in-plane skyrmion boundary. This last observation is due to the role of the Néel caps as a flux-closure structure and may indicate an approach to increase skyrmion stability by designing heterostructures with artificial soft layers. Understanding this structure may allow other skyrmion materials to be augmented in such a way as to increase their stability, or alternatively, design the topology in artificial magnetic systems. The approach used here ties together the observed neutron scattering results to magnetic configurations which are constrained by their underlying physics, providing an improved investigative paradigm which can be leveraged to achieve an enhanced understanding of other magnetic systems.

Chapter 4

Skyrmion lattice formation and destruction mechanisms probed with SANS

4.1 Introduction

As noted in the introduction, skyrmions in B20 materials tend to form ordered hexagonal lattices, with sizes that are determined by the balance between different magnetic energies. The competition between exchange interactions and DMI leads to the curling of magnetic moments and form the skyrmion in an external magnetic field at a given temperature. One important fundamental question how fast a skyrmion lattice is construct or destruct in a given magnetic material. One study conducted by L. J. Bannenberg *et al.*[16], has demonstrated that reorientation of skyrmion lattice relative to a magnetic field takes hundreds of seconds. This suggests that skyrmion lattice dynamics may be much slower than in traditional domain walls, which can form in nanoseconds or picoseconds. In a different study, M.N.Wilson *et al.*[11] used electric fields to nucleate a magnetic skyrmion lattice in zinc substituted Cu_2OSeO_3, finding that the lattice forms over several milliseconds, and the energy barrier of formation is in the meV range [11]. These time scales are a surprise as one expects skyrmion lattice dynamics to occur at much faster timescales (ns of ps). The above research investigates the skyrmions dynamic time scales by using indirect mechanisms (reorientation or use the electric field), and not revealing direct information about the time constants of construction or destruction of skyrmion lattice.

Small angle neutron scattering (SANS) is a powerful non-destructive tool for reciprocal space-based studies of magnetic systems. In bulk B20 materials, the skyrmions form an ordered hexagonal lattice which generates a hexagonal diffraction pattern in SANS measurements; therefore, by measuring the diffraction pattern versus time during the formation and destruction of the lattice, the dynamics and timescales of lattice formation can be measured. Time-resolved SANS (TSANS) experiments at NIST's Center for Neutron Research (NCNR) is a neutron technique to achieve sub-millisecond time resolutions in SANS measurements, and also a novel and effective technique to study the dynamics in magnetic structures.

In this study we used TSANS in three different B20 bulk materials (MnSi, Cu_2OSeO_3, $Fe_{0.85}Co_{0.15}Si$) to investigate the construction and destruction dynamics of skyrmion lattices. The experiment was performed by rapidly stepping the magnetic field that is parallel to the neutron beam, such that the system is pushed into and out-of the skyrmion stabilizing pocket resulting in lattice formation and destruction, respectively. We use a variety of fields, field steps and temperatures to probe the formation and destruction dynamics at various points within the skyrmion stability pocket to achieve a comprehensive understanding about the changing magnetic configuration and timescales. The present study demonstrated that creation and destruction time scales are in millisecond time scale ranges and a variety of dependencies of the dynamics on field, temperature, and the underlying material properties.

4.2 Methods

Bulk single crystal MnSi, Cu_2OSeO_3 (COSO), and $Fe_{0.85}Co_{0.15}Si$ (FCS) samples were used for the experiments, and were prepared as described previously [36, 58, 37]. Neutron scattering experiments were performed using the NG7 beamline at NCNR [20]. An unpolarized neutron beam with a wavelength (λ) of 6 Å ($\Delta\lambda/\lambda$ = 13%) was used. Each sample was cooled in a closed cycle refrigerator to the measurement temperature and placed within an electromagnet, with the field aligned along the neutron beam direction. A second coil is placed around the sample, with the coil axis also parallel to the neutron beam, which is used to apply the rapidly changing step field. Samples were mounted on a B:Al sample stage, with Cd mask to reduce background scattering (Fig. 4.1).

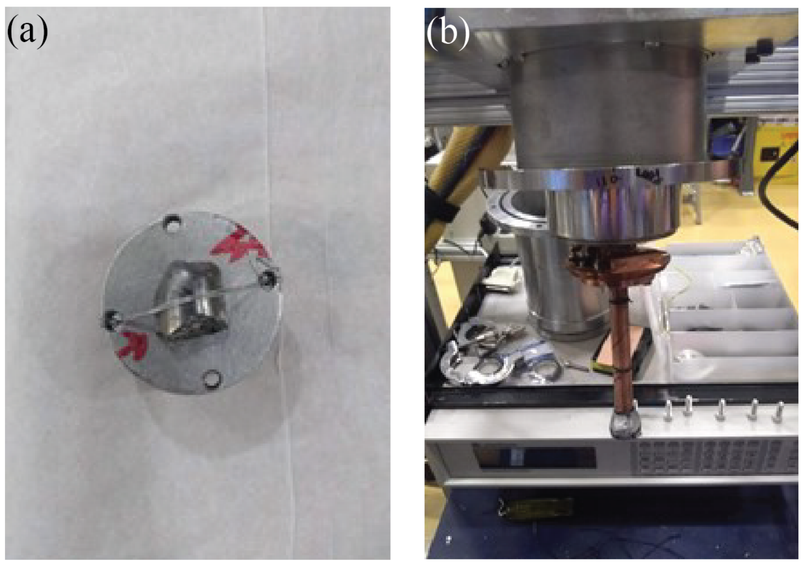

Figure 4.1: Experiment setup in vSANS instrument (a) sample (MnSi) attached to the sample holder. (b) sample holder attached to the cryogenic cold head.

Once the sample is cooled to the measurement temperature, the static field is increased until a hexagonal diffraction appears in the SANS detector, indicating the boundary of the skyrmion stability pocket. Then the magnetic field is stepped by using a square current pulse of 0.1 Hz by using the secondary coils, switching between positive and negative polarity, such that the magnetic field is outside\inside the stabilizing pocket to destroy\create the skyrmion lattice (Fig. 4.2). Each neutron count was tabulated and included a timestamp with approximately nanosecond resolution. For each measurement, SANS data was collected continuously for up-to 2 hours. The data was then averaged over 10 second period representing the 0.1 Hz field, similar to a lock-in amplifier, then further discretized into 10 ms frames. For each time frame the average integrated intensity was calculated for an annular ring which covers the hexagonal diffraction pattern in the detector. Igor [59] and Grasp softwares were used to reduce the data and subtract the background. Creation\destruction time constants are calculated by fitting sigmoidal or exponential functions for the intensity vs. time graphs, as discussed below.

4.3 Results

4.3.1 MnSi

As the first sample, MnSi is used. MnSi belongs to the space group P_{213}, with a lattice constant of 4.56 Å [17]. Previous studies have shown that MnSi undergoes a magnetic phase transition just below the curie temperature, Tc, of 29.5 K [17]. In

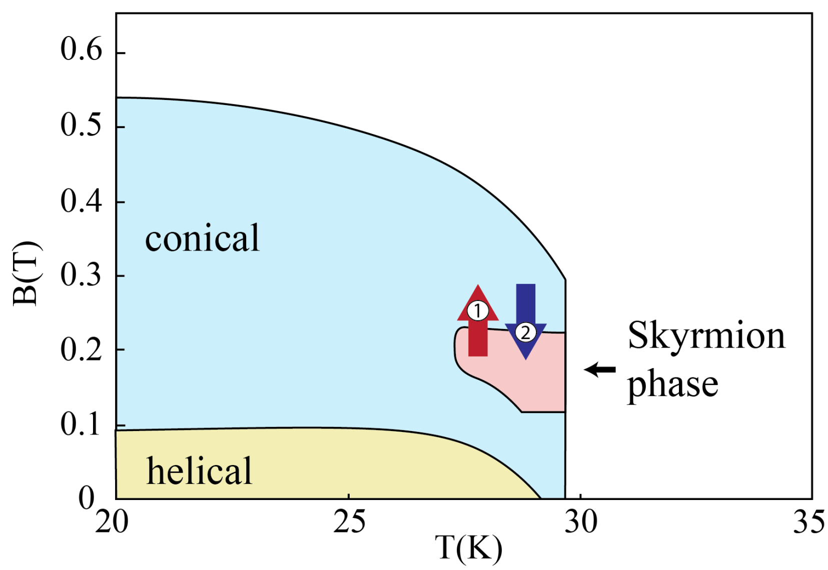

Figure 4.2: The B-T phase diagram for MnSi [11] was examined in this experiment. The field was incrementally increased to push the skyrmion lattice out or into the stabilized window, leading to its destruction (indicated by the red arrow) or creation (indicated by the blue arrow), respectively. Each measurement involved step 1, where the field was increased (decreased) following the red arrow, and step 2, where the field was subsequently decreased (increased) following the blue arrow in the B-T phase diagram.

the MnSi B-T phase diagram, skyrmions exist within a small pocket of temperatures between Tc and 27.5 K, and magnetic field between 100 mT to 250 mT. The sample showed the transition from helical to conical and the skyrmion state [10, 17] as the temperature increased.

The MnSi sample was ZFC to the test temperature (28.8 K, just below T_c) then a static magnetic field aligned with the neutron beam and [110] axis of the MnSi crystal, was applied. The field was increased to 250 mT, which corresponds to the high field boundary of the skyrmion pocket; at this field a 6-fold pattern is observed on the SANS detector which disappears at higher fields. A hexagonal scattering pattern was observed at q = $(3.8 \pm 0.1) \times 10^{-2}$ Å^{-1} (Fig. 4.3a), corresponding to the real space skyrmion lattice spacing of 165 ± 4 Å. Some peaks appeared brighter due to a misalignment between the crystallographic direction of the sample or magnetic field and the neutron beam.

A bipolar square wave field was then applied with a magnitude of ±12.5 mT and the time-resolved SANS pattern was captured; measurements were also performed with a field of ±37.5 mT. These fields move the state across the high field boundary of the skyrmion pocket. The field is rapidly increased from 250 mT to 262.5 mT and the hexagonal pattern disappears from the SANS detector (Fig. 4.3b), confirming that the sample was out of the skyrmion pocket. Next, 5 seconds later, the magnetic field is decreased to 237.5 mT and the hexagonal patter returns, indicating the system is back within the skyrmion stability pocket. Similar observations were made with the field of ± 37.5 mT, however it is notable that the scattering intensity at 212.5 mT

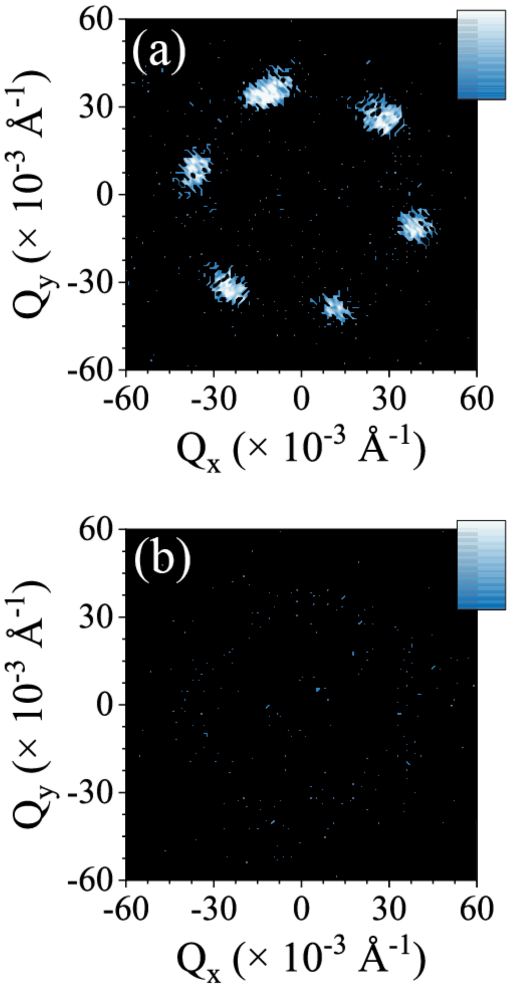

Figure 4.3: (a) The 2D small-angle neutron scattering (SANS) pattern obtained from the MnSi sample revealed a hexagonal scattering pattern at (3.8) $\times 10^{-2}$ Å^{-1}, corresponding to a skyrmion lattice size of 165 Å. The magnetic field used during the measurement was 237.5 mT. (b) In the conical phase of the MnSi sample, which is outside the skyrmion stabilized window, the hexagonal SANS pattern disappeared from the detector.

was larger than at 237.5 mT, despite both being within the skyrmion stability pocket. This may indicated domains within the sample which have not transformed to the skyrmion state at 237.5 mT, or that the shape of the skyrmion, which contributes the scattering form factor, is different.

Following the sequence discussed in the Methods section, the time resolved diffraction pattern is determined and the intensity vs. time graphs calculated. A stepwise exponential function was used to fit the change in diffraction intensity and determine the time constants for the creation and destruction of the skyrmion lattice. For the destruction of the skyrmion lattice (Fig. 4.4a) the following functions were used:

$$\begin{aligned} &c + d && ; t < t_0 \\ &c\left(e^{-\frac{(t-t_0)}{\tau}}\right) + d && ; t \geqslant t_0 \end{aligned} \tag{4.1}$$

Also, for the formation of the skyrmion lattice, the following functions were used (Fig. 4.4b).

$$\begin{aligned} &d && ; t < t_0 \\ &c\left(1 - e^{-\frac{(t-t_0)}{\tau}}\right) + d && ; t \geqslant t_0 \end{aligned} \tag{4.2}$$

In the above functions c represents the intensity from the skyrmion lattice, t_0 is the measurement time when the field changes, τ is formation or destruction time constant, and d is the background intensity, respectively. The critical parameter we consider here is the time constant (τ).

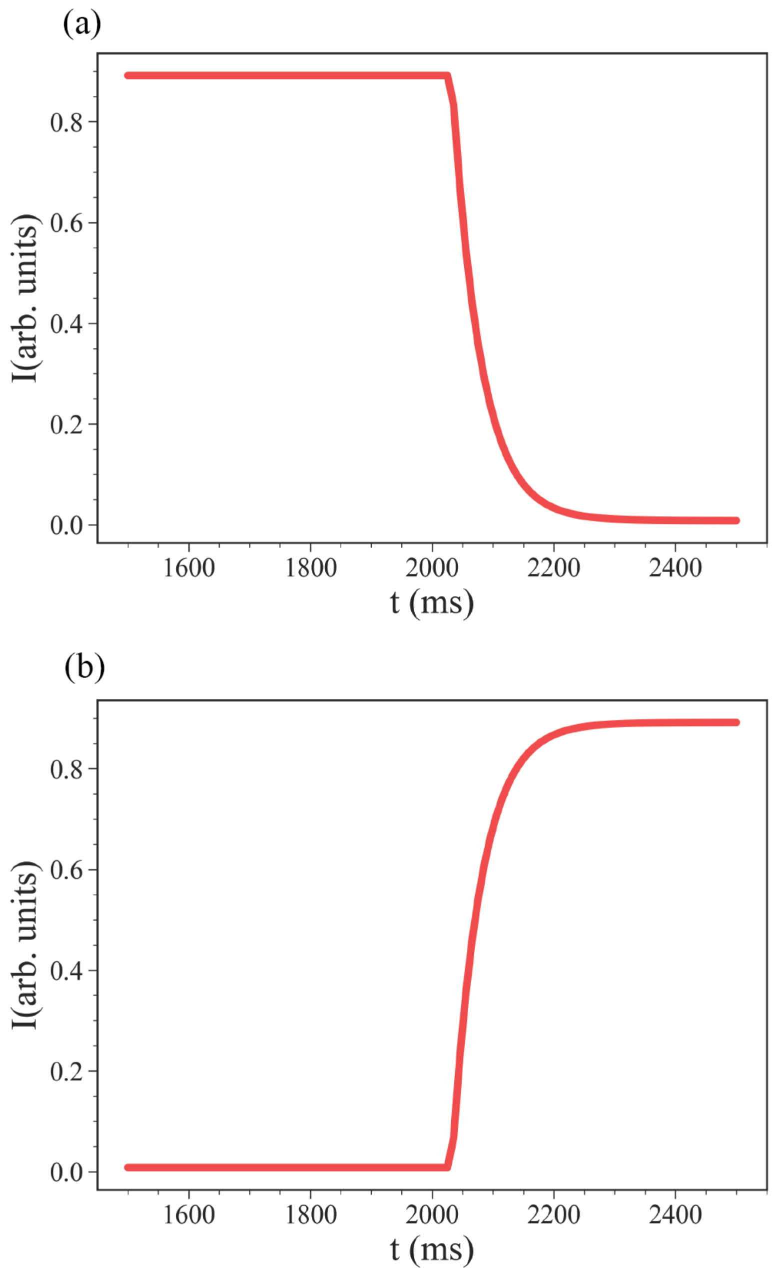

Figure 4.4: exponential functions used to fit the data for (a) destruction (b) formation of skrmion lattice.

The converged value for τ is 42.71 $\pm$ 0.03 ms for MnSi, with a field step of $\pm$ 12.5 mT, centered at the top boundary (250 mT)(Fig. 4.5). Taking a smaller field step (288 mT to 212 mT) increased τ to 47.8 $\pm$ 0.05 ms. These values show that increasing the field step size causes the time constant for skyrmion lattice formation at the upper boundary to decrease. The converged values at this same boundary for skyrmion lattice destruction are much faster, with τ = 18.0 $\pm$ 0.01 ms and 10.36 $\pm$ 0.03 ms for field steps of (237 mT to 263 mT) and (212 mT to 288 mT) (Fig. 4.5), respectively.

At the lower boundary of the skyrmion stability pocket (160 mT) the formation time constant was determined to be 21.4 $\pm$ 0.1 ms for a field step of (122 mT to 198 mT), notably faster than the upper boundary. Skyrmion lattice destruction time constant is 18.97 $\pm$ 0.02 ms for the field step size of (198 mT to 122 mT).

For the complementary field step taken at the lower field boundary (148 mT to 172 mT) the hexagonal diffraction pattern does not disappear from the SANS detector, indicating that the magnetic field is not entirely outside of the skyrmion pocket. Surprisingly, the destruction and formation time constant for a field change of $\pm$12.5 mT was very significant (50.9 $\pm$ 0.03 ms and 44.32 $\pm$ 0.05 ms, respectively). This data shows a longer relaxation process in the intensity versus time graph after changing the magnetic field. The data for all of the formation and destruction timeframes in MnSi and other skyrmion materials are included in Table 1.

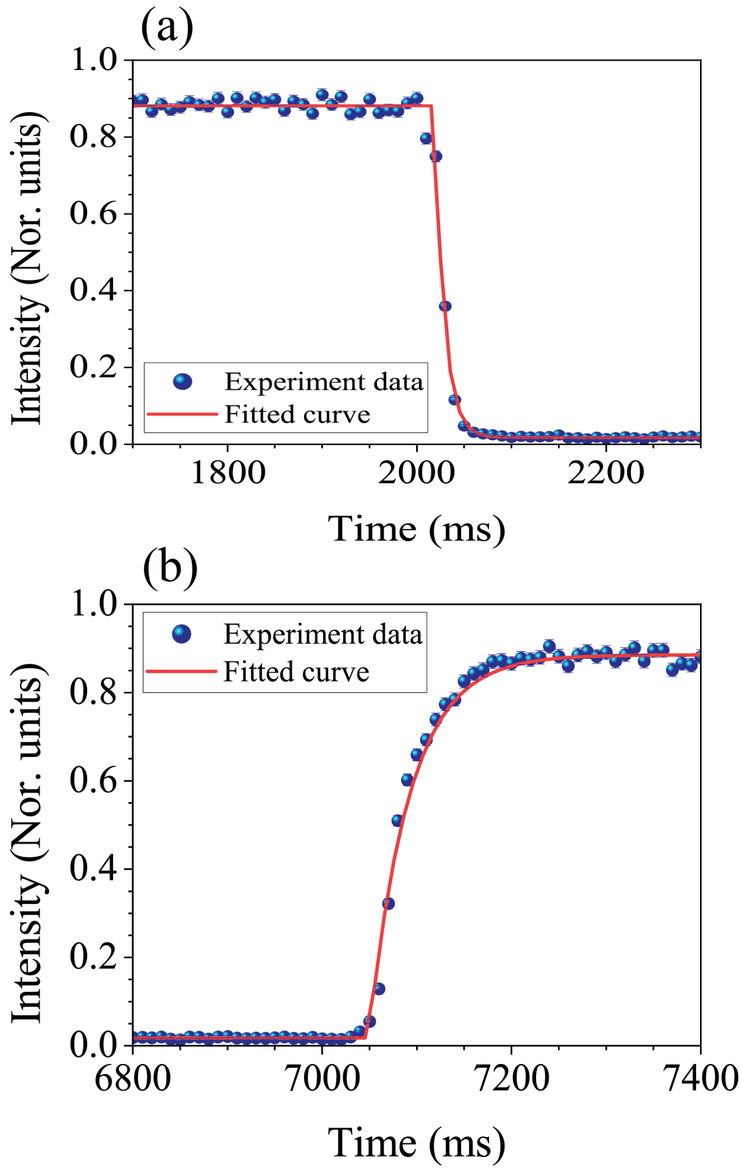

Figure 4.5: The graph illustrates the normalized averaged scattering intensity in the azimuthal direction of the scattering pattern plotted against time for the destruction and construction of the skyrmion lattice.

4.3.2 $Fe_{0.85}Co_{0.15}Si$

For the second experiment of this work, the formation and distruction times of the skyrmion lattice was measured in single crystal $Fe_xCo_{1-x}Si$ (x=0.85). This material provides a complementary skyrmion lattice with a different interskyrmion spacing, temperature and field ranges, as well as the underlying exchange-constants. As another traditional B20 magnetic material, FCS shows a skyrmion lattice near the Curie temperature of ≈20 K.[60, 61, 12] The sample was cooled in zero magnetic field (ZFC) to 20.5 K, then a magnetic field was applied parallel to the neutron beam in the [001] direction. This establishes a skyrmion lattice with one of the the major axes along the [100] direction, consistent with previous works [62, 63]. Using the procedure described in the methods section, the formation and destruction of the skyrmion lattice is observed with SANS and the time constants are calculated for the two magnetic field steps (±10 mT and ±5 mT) at 20.5 K.

Similar to MnSi, the FCS sample was ZFC to the measurement temperature (20.5 K) then the magnetic field was increased in small steps, until a clear hexagonal diffraction pattern appeared (20 mT), then further increased until the hexagonal pattern disappeared (55 mT). These fields were identified as the lower- and upper-field boundaries of the skyrmion stability window. Next, at the upper field boundary, the stepped field of ±10 mT is applied, spanning between 45 mT to 65 mT. The scattering pattern does not reproduce the hexagonal feature observed after the ZFC sequence, despite being within the skyrmion stability envelope. Rather, the scattering pattern measured at μ_0H=45 mT, shown in Fig. 4.6a, appears as an inhomogeneous ring with a radius q = (1.53 ± 0.1) $\times 10^{-2}$ Å^{-1}, corresponding to a real space skyrmion lattice constant of 410 ± 28 Å. The appearance of a ring inside of the skyrmion stability envelope suggests that the skyrmions form with short range order but no long-range orientation between domains. Following the measurement sequence, the field was stepped to 65 mT, at which point the diffraction pattern disappears (Fig. 4.6b); stepping the field back to 45 mT, the ring reappears. The intensity of the diffraction pattern was once-more extracted from each 10 ms frame and the creation and destruction time constants calculated. Time constants for the formation and destruction of the skyrmion lattice were determined to be 70.28 ± 0.06 ms and 35.49 ± 0.03 ms for field steps of ±10 mT and 72.1 ± 0.06 ms and 58.28 ± 0.05 ms for smaller field steps of ±5 mT.

Data was also collected at the lower boundary of the skyrmion stability envelope, centered at 20 mT with the field steps of ±5 mT and ±10 mT. At both 25 mT and 30 mT the system is inside the skyrmion stability envelope and the scattering pattern shows a hexagon imposed over a uniform ring (Fig 4.6c). As the measurement field steps to lower fields, outside of the skyrmion stability envelope, the scattering pattern mostly disappears, however two weak diffraction peaks are observed along the Q_y direction (Fig. 4.6d). These two peaks indicate a helix structure along the Y-direction. Time constants for the formation and destruction of the skyrmion lattice at the lower field boundary were measured to be 71.19 ± 0.05 ms and 20.22 ± 0.03

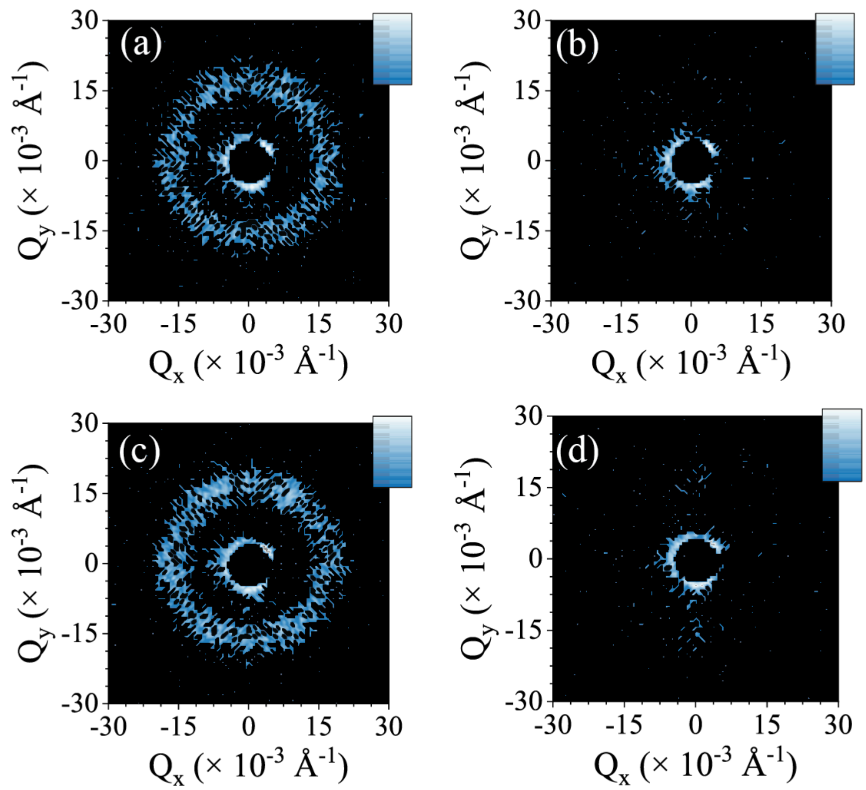

Figure 4.6: SANS data for FCS sample (a) Ring type scattering pattern is visible in the detector. (b) Scattering for sample in the conical phase (c) At lower boundary 2D SANS pattern shows a hexagon imposed over a uniform ring (d) At lower boundary out of skyrmion stabilizing envelope weak diffraction peaks are observed along the Qy direction

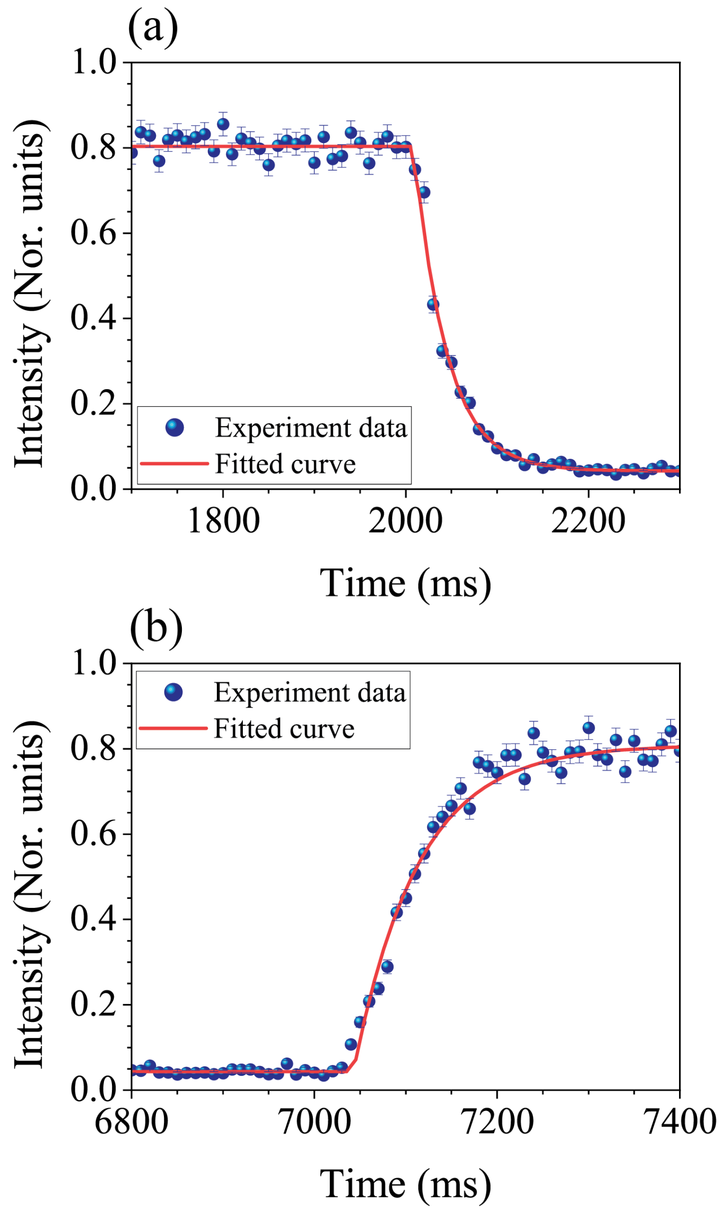

Figure 4.7: The graph illustrates the normalized averaged scattering intensity in the azimuthal direction of the scattering pattern plotted against time for (a) the formation and (b) destruction of the skyrmion lattice.

ms for the field step of ±10 mT and were 98.99 ± 0.07 ms and 39.16 ± 0.04 ms for a field step of ±5 mT.

A third field sequence was performed on the FCS, using a field of 27 mT with a step of ±5 mT. Using this field range, both the maximum (32 mT) and minimum (22 mT) field are within the skyrmion stability pocket. At 32 mT the scattering pattern resolves to a hexagon imposed over a uniform ring, while at 22 mT the pattern is simply a hexagon. This could imply that, at the higher field, the skyrmion lattice is dephasing and losing long-range orientation. Alternatively, this could imply that the skyrmion lattice is dissolving to become skyrmions plus helices. Interestingly, the total integrated scattering intensity of these two states is conserved suggesting that the scattering is a result of the same structure and dephasing is likely occurring; if helices were formed, the scattering form factor would change, resulting in a different intensity. Measurements performed on this sample previously [53] have observed a ring plus hexagon scattering pattern which was resolved to a hexagon by rotating the sample in a static field, further supporting the conclusion that the ring originates from misoriented skyrmion domains. Time constants for dephasing of the skyrmion domains is reported to be 38 ms (for a step of 32 mT to 22 mT) while the reorientation to a single-domain configuration occurs in 58 ms (for a step of 22 mT to 32 mT). We note that these time constants are significantly different from the case where the skyrmions were explicitly created and destroyed.

4.3.3 Cu_2OSeO_3

The Cu_2OSeO_3 (COSO) sample exhibits a magnetic phase transition in the B-T phase diagram at approximately 58 K, close to its Curie temperature. Within this temperature range, skyrmions are formed in a stability window spanning from 55 K to 58 K. [64] Previous investigations on COSO have demonstrated its high sensitivity to slight variations in external fields and temperatures, including the observation of multi-domain skyrmion lattices and the presence of two distinct skyrmion phases at different temperatures. [16, 65, 47, 14] In comparison to the other materials examined in this study, COSO exhibits the shortest time constants.

Measuring at 57 K, a hexagonal scattering pattern appears at q = $(9.73 \pm 0.08) \times 10^{-3}$ Å^{-1} and a magnetic field of 17 mT (Fig 4.8a) then disappears, under a slowly increasing magnetic field, at 33 mT, corresponding to the lower and upper boundaries of the skyrmion stability envelope, respectively. Using a $\pm$10 mT stepped field centered at 33 mT, the scattering pattern evolved between a hexagon at 23 mT, and no appreciable scattering at 43 mT (Fig 4.8b). This indicates that the system transforms unambiguously from the skyrmion state to a non-skyrmion, likely the conical state based on previous reports. From the scattering intensity, the creation and destruction time constants were measured to be 26.8 $\pm$ 0.09 ms and 29.59 $\pm$ 0.09 ms. Compared to the other samples, this is much faster, and the creation and destruction timescales more symmetric. Investigating the lower boundary of the skyrmion stability envelope, the field was stepped between 7 mT and 27 mT, transitioning between a hexagon at

27 mT and no-appreciable scattering at 7 mT. From this data, the skyrmion lattice creation and annihilation time constants were measured as 37.1 ± 0.1 ms and 18.48 ± 0.08 ms, respectively. This is still faster than the other samples, but now shows the asymmetry in lattice formation and destruction times (4.8 c-d).

The time constants for all of the discussed creation and annihilation measurements discussed in this text are summarized in Table 4.1.

4.4 Discussion

This study investigates the ordering timescales for three different B20 skyrmion bulk materials: MnSi, FCS, and COSO. The SANS results show that the skyrmions form ordered hexagonal lattices over a surprisingly long timeframe (10's of miliseconds) and that these timeframes vary significantly between the three samples, with the fastest single events being 10.4 ms (MnSi, skyrmion lattice destruction at the upper field boundary), and the slowest being 99 ms (FCS skyrmion lattice formation at the lower boundary). The formation and destruction timeframes from all of the measurements are tabulated in Table 4.1. While there is no absolute trend, following the average, COSO is the fastest, while FCS is the slowest, and MnSi is in-between, when taking a common field step of ≈10 mT.

The formation and destruction mechanics can be investigated in detail by evaluating the time-resolved structure of the diffraction peaks. Specifically, the peaks in the SANS pattern encode the average structure of the skyrmion lattice,

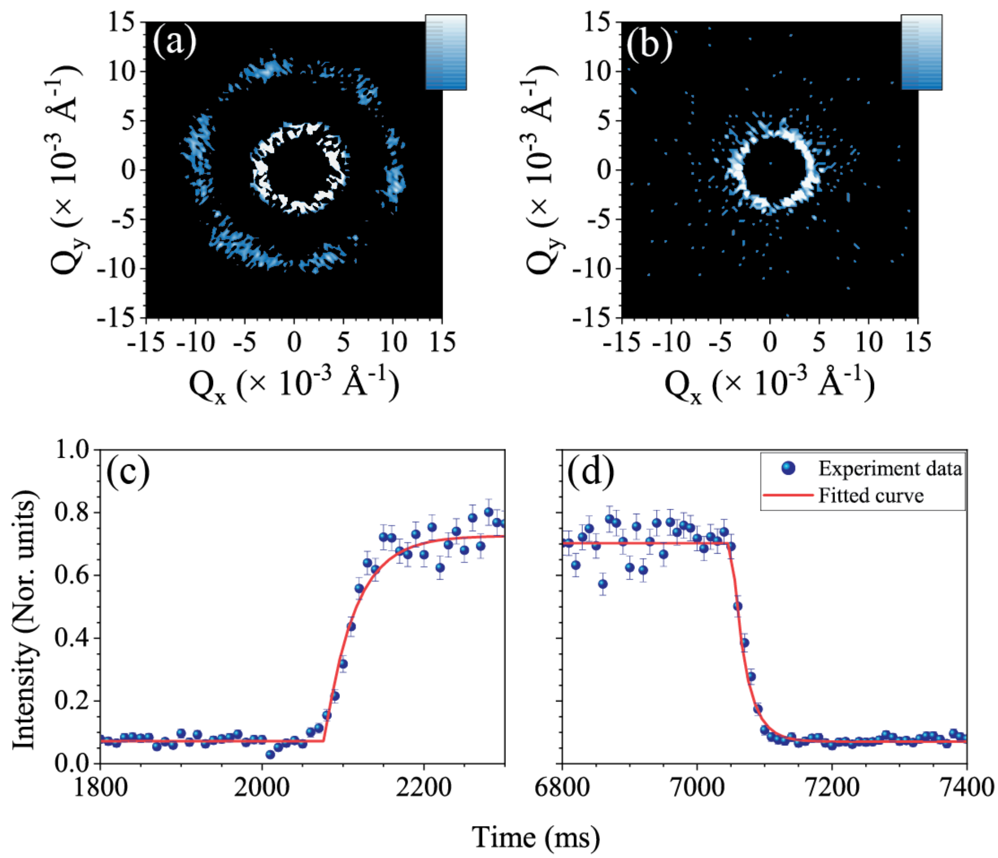

Figure 4.8: SANS patterns of Cu_2OSeO_3 taken at (a) 23 mT field and (b) 43 mT field Graphs depicting the normalized averaged scattering intensity in the azimuthal direction over time, illustrating (c) the formation and (d) destruction of the skyrmion lattice.

Table 4.1: Summary of the formation and destruction time constants with uncertainties for three samples. These data contains values for larger field steps.

Sample	**T(K)**	**State change**	**Formation\Destruction**	$\mathbf{H_i \rightarrow H_f (mT)}$	$\boldsymbol{\tau}$**(ms)**	$\boldsymbol{\Delta\tau}$**(ms)**
MnSi	28.8	skx → conical	Destruction	212.5 → 287.5	10.36	0.03
		conical → gkx	Formation	287.5 → 212.5	42.71	0.04
		skx → conical	Destruction	237.5 → 262.5	18.01	0.05
		conical → kkx	Formation	262.5 → 237.5	47.78	0.04
		conical → skx	Formation	122.5 → 197.5	21.4	0.1
		skx → conical	Destruction	197.5 → 122.5	18.97	0.02
		conical → skx	Formation	147.5 → 175.5	44.32	0.05
		skx → conical	Destruction	175.5 → 147.5	50.9	0.025
FCS	20.5	skx → conical	Destruction	45 → 65	35.49	0.03
		conical → skx	Formation	65 → 45	70.28	0.06
		skx → conical	Destruction	50 → 60	58.29	0.05
		conical → skx	Formation	60 → 50	72.1	0.06
		helical → skx	Formation	10 → 30	71.19	0.05
		skx → helical	Destruction	30 → 10	20.22	0.03
		helical → skx	Formation	15 → 25	98.99	0.07
		skx → helical	Destruction	25 → 15	39.15	0.04
COSO	57	skx → conical	Destruction	23 → 43	29.55	0.09
		conical → skx	Formation	43 → 23	26.8	0.09
		conical → skx	Formation	7 → 27	37.12	0.1
		skx → conical	Destruction	27 → 7	18.48	0.09

with the peak location, e.g. radius (q), related to the inter-skyrmion spacing by the relationship $d = \frac{2\pi}{q}$ and the azimuthal angle corresponding to the long-range orientation of the hexagonal lattice. Naturally, variations in the lattice spacing will appear as directional broadening of the peak in the radial direction, with larger real-space structure corresponding to smaller q, while variations in the lattice orientation appear as a broadening in the azimuthal direction. These trends are tabulated for an example case of MnSi at 28.8 K and a field step of 287.5 mT to 212.5 mT, corresponding lattice formation at the high-field boundary of the stability pocket. The peak location, Fig. 4.9a, shows a slight increase with ordering time, indicating that the skyrmion lattice initially forms with a larger spacing than the static configuration. Translating these values to real-space lattice parameters, the inter-skyrmion spacing when first observed is 173 Å and quickly relaxes to its final value of 165 Å, a change of <5%. This is consistent with established understanding that the skyrmion lattice period is determined by the ratio D/J, which does not change as the lattice is formed [66]. However, it is interesting to note that the peak width along the radial direction (Δq) has a much more significant change, Fig. 4.9c, decreasing by <70% during the formation process. The peak width was approximately symmetric, implying that domains initially nucleate with much larger and smaller lattice parameters. This could indicate that skyrmions with a diameter of ≈165 Å form but suffer from a diminished packing factor, or more likely, that skyrmions which are particularly large or small nucleate to form a local domain.

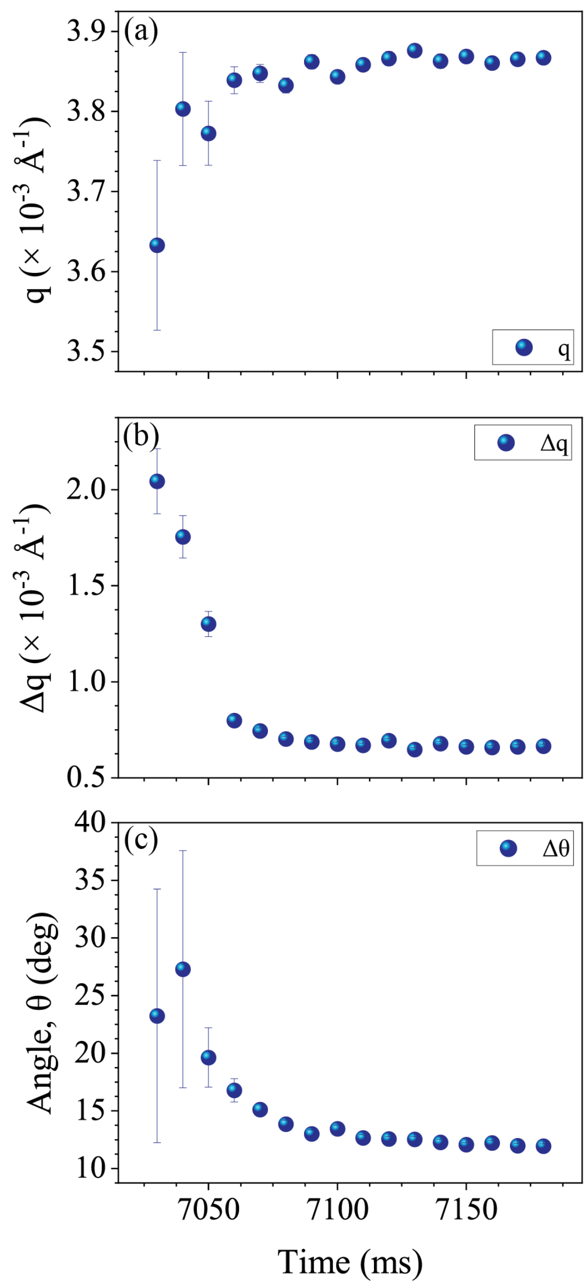

Figure 4.9: Example trends, taken from MnSi at 28.8 K and a field step of 287.5 mT to 212.5 mT, corresponding to lattice formation and showing (a) the peak position and (b) width in q and (c) the peak width in the azimuthal direction.

Finally, the azimuthal distribution, Fig. 4.9c, also shows a decreasing trend, with the peak width decreasing by ≈50%, from 25° to 12°, during the formation. A width of 25° is notable since the spacing between diffraction peaks is nominally 60°. This last trend suggests that the system initially nucleates several domains of ordered skyrmions with poor relative alignment, and as the ordering propagates, the relative orientation improves considerably. Since the magnetic field is applied along the skyrmion tubes, the in-plane orientation of the skyrmion lattice is determined by coupling to the underlying crystal lattice through the magnetocrystalline anisotropy. In these materials, the magnetocrystalline anisotropy is notably weak resulting in the poor initial ordering, but alignment improves as the domains grow and eventually intersect.

Considering now the timescales of lattice formation, there are many underlying factors which may influence the formation and destruction timeframes of the skyrmion lattice. These factors include the no-less than four energy terms (exchange, DMI, magnetostatic, and magnetocrystalline), two dependent variables (magnetic field and temperature) and two variables that are challenging to control or quantify (chemical disorder, and defect density). To help elucidate the underlying physics, the timescales for field step are considered within each material, then using the 10 mT step as a fixed variable, comparisons are made between materials using the parameters tabulated in Table 4.2 for MnSi [67, 68, 69], COSO [70, 71], FCS [36, 61, 72]

For each material the data shows that a larger field step results in a faster the formation/destruction timeframe. For FCS the average formation and destruction

Table 4.2: Saturation magnetization, exchange stiffness, DMI constant values for each of the sample and the interskyrmion distance (skyrmion lattice size). SM = semimetallic, Insul=insulator.

Sample	**Saturation Magnetization - M_s ($\times 10^5$A/m)**	**Exchange Stiffness ($\times 10^{-13}$J/m)**	**DMI ($\times 10^{-5}$J/m^2)**	**Magnetocrystalline anisotropy ($\times 10^3$J/m^3)**	**Skyrmion lattice size (Å)**	**D/A (nm^{-1})**	**Resistivity atT_C ($\mu\Omega$cm)**
MnSi	1.63	8.44	21.6	17	164	0.406	29
$Fe_{0.85}Co_{0.15}Si$	9.08	6.01	7.97	180	410	0.133	331
Cu_2OSeO_3	1.03	7.00	7.4	-0.6	645	0.106	Insul.

timeframe was 71 ms and 28 ms for the 20 mT field step, and 86 ms and 49 ms for a 10 mT step, respectively. Also, for the MnSi, the average formation and destruction timeframe was 32 ms and 15 ms for a 75 mT step and 46 ms and 34 ms for a 25 mT step. This can be easily understood by recognizing that the particular magnetic configuration is determined by the balance of the Zeeman (field) energy and the other energies within the system, including thermally induced fluctuations. Moving the field such that the system is far from equilibrium increases the energy difference between the instantaneous configuration and the thermodynamically stable arrangement. In this condition, the smaller thermal fluctuations will be sufficient to nucleate domains which will propagate faster as a result of the larger energy difference. Notably, there is little dependence on the central field of the transition, that is, whether the transition is at the upper or lower field boundary.

Comparing now between materials, for approximately the same field step, higher temperatures result in faster ordering. Specifically, the average ordering times (average of formation and destruction) were 28 ms, 40 ms and 49 ms for COSO (T=57 K, ΔH= 20 mT), MnSi (T=28 K, ΔH= 25 mT) and FCS (T=20 K, ΔH= 20 mT), respectively. This may emphasize the critical role that thermal fluctuations play in the ordering dynamics.

Comparing the trend in the speed (fastest to slowest, 28 ms, 40 ms, and 49 ms, COSO, MnSi, FCS) with Table 4.2, two more trends appear: (1) the formation time increases with the saturation magnetization (1.03 A/m, 1.63 A/m and 9.08 A/m for COSO, MnSi and FSC, respectively) and (2) the magnetocrystalline anisotropy (0.6 J/m^3, 17 J/m^3 and 180 J/m^3 for COSO, MnSi and FSC, respectively). The dependence on the saturation magnetization is surprising, since each of the magnetic energies are linearly related to the magnetization (or spin); raising MS raises all of the energies. For the magnetocrystalline energy, one can consider the energy necessary to propagate the skyrmion lattice necessitates rotating spins through a magnetic hard axis. This effect was reported previously in multilayers with perpendicular anisotropy, that reducing the anisotropy increased the domain wall creep velocity [73].

Finally, we consider the role of disorder in the system, in this case chemical inhomogeneity. While both MnSi and COSO are expected to be chemically homogeneous, the FSC sample has inherent disorder on the A-site, having a weighted random occupation of Fe and Co. This distribution can pin the skyrmions, slowing the ordering mechanics [74]. Indeed, FCS has the slowest ordering time.

At this point it is important to note that the dependence on the remaining variables may be convoluted with other parameters, or simply too small in the current systems, and may be dominant in other materials. With this in mind, it is interesting to reflect on the parameters which do not have a clear trend in the formation and destruction in these data and why they should. First among these are the exchange and DMI terms, both of which are largest in MnSi, the medium speed material. Similar to the magnetic field arguments, these terms increase the energy scale of the system such that being out of equilibrium presents a significant energy cost and should motivate rapid lattice formation and destruction. The ratio D/J determines the skyrmion size, which also intuitively affect the ordering timeframes. Specifically, re-configuring large domains will take longer both due to their size, but also an inability to move freely between other skyrmions, however, MnSi has the smallest skyrmions, despite being having the medium speed.

Another variable which might be expected to play a role in the ordering is the central field of the transition, corresponding to the upper or lower field transition. For the MnSi, the average ordering time at the upper field boundary is faster, while in FSC the lower field boundary is faster, and for COSO the ordering times are approximately the same. Knowing that the field step plays an important and unambiguous role, the upper field boundary might be expected to be faster. Alternatively, the upper field boundary is changing between the skyrmion state and a highly distorted conical structure, while the lower field boundary is transitioning to a much more relaxed conical – or even helical – state; resolving to different configurations might be expected to take different times.

4.4.1 Conclusion

In summary, we have used time-resolved small angle neutron scattering (SANS) to investigate the ordering dynamics in three prototypical B20 skyrmion materials: MnSi, $Fe_{0.85}Co_{0.15}Si$ and Cu_2OSeO_3. The scattering pattern shows that the ordering of the skyrmion lattice evolves asymptotically towards the stable configuration over a surprisingly slow timeframe of 10 ms - 100 ms. Trends were observed in the data: taking larger field steps and transitioning at higher temperatures increased the ordering speed. These observations may indicate the role of thermal fluctuations within the system. Also, the with increasing saturation magnetization and magnetocrystalline anisotropy the ordering speed was reduced. Identifying and understanding these ordering timeframes are important for technological applications, particularly if the proposed technology relies on a skyrmion lattice. This work also presents interesting fundamental qualities, since this magnetic order is much smaller than typical magnetic dynamics or domain wall motion.

Chapter 5

Conclusions

In conclusion, these studies focused on the investigation of different types of skyrmion systems using neutron scattering techniques. The 3D structure of the hybrid skyrmion in the Fe/Gd multilayer system was determined, shedding light on important aspects of its construction. The study successfully employed a combination of neutron scattering and physics-based modeling, offering an improved investigative approach to gain deeper insights into magnetic systems and enhance stability in other skyrmion materials.

Furthermore, this study explored the dynamics of the skyrmion lattice in traditional B20 magnetic materials, namely MnSi, FCS, and COSO. These materials exhibited distinct magnetic dynamics in terms of skyrmion lattice ordering, influenced by various factors including magnetic parameters and thermal contributions.

The effects of temperature and different magnetic energy terms on the formation and destruction time scales of the skyrmion lattice were also investigated. The results indicated that increasing temperature led to decreased time constants for formation and destruction, allowing greater freedom for magnetic moments to fluctuate and respond to external magnetic fields. Also higher magnetocrystalline anisotropy results in higher formation and destruction time constants.

In summary, this study not only provided insights into the structure and dynamics of hybrid skyrmions but also expanded our understanding of traditional B20 skyrmion materials. The findings contribute to the exploration of magnetic systems and offer valuable knowledge for the development of stable skyrmion materials and the manipulation of their properties, including the time scales associated with the formation and destruction of skyrmion lattices.

Bibliography

[1] Albert Fert, Vincent Cros, and João Sampaio. Skyrmions on the track. *Nature Nanotechnology*, 8(3):152–156, 2013. xiii, 5, 6

[2] S. Mühlbauer, B. Binz, F. Jonietz, C. Pfleiderer, A. Rosch, A. Neubauer, R. Georgii, and P. Böni. Skyrmion lattice in a chiral magnet. *Science*, 323(5916):915, 2009. xiii, 6, 8

[3] Ryan D. Desautels, Lisa DeBeer-Schmitt, Sergio A. Montoya, Julie A. Borchers, Soong-Geun Je, Nan Tang, Mi-Young Im, Michael R. Fitzsimmons, Eric E. Fullerton, and Dustin A. Gilbert. Realization of ordered magnetic skyrmions in thin films at ambient conditions. *Physical Review Materials*, 3(10), 2019. xiv, 10, 27, 31, 32, 33, 34, 43

[4] C. Ulrich. Magnetic neutron scattering and spin-polarized neutrons. 2005. xix, 111

[5] Hans Christoph Siegmann Joachim Stöhr. *Magnetism*. Springer, Berlin, Heidelberg, 1 edition, 2006. 1

[6] C. D. Graham B. D. Cullity. *Definitions and Units*, pages 1–21. Wiley Online Books. John Wiley Sons, Ltd, 2008. 2

[7] T. H. R. Skyrme. A unified field theory of mesons and baryons. *Nuclear Physics*, 31:556–569, 1962. 4

[8] T. H. R. Skyrme and William George Penney. Particle states of a quantized meson field. *Proceedings of the Royal Society of London. Series A. Mathematical and Physical Sciences*, 262(1309):237–245, 1961. 4

[9] F. Jonietz, S. MÃ¼hlbauer, C. Pfleiderer, A. Neubauer, W. MÃ¼nzer, A. Bauer, T. Adams, R. Georgii, P. BÃ¶ni, R. A. Duine, K. Everschor, M. Garst, and A. Rosch. Spin transfer torques in mnsi at ultralow current densities. *Science*, 330(6011):1648–1651, 2010. 6

[10] A. Neubauer, C. Pfleiderer, B. Binz, A. Rosch, R. Ritz, P. G. Niklowitz, and P. Böni. Topological hall effect in the *a* phase of mnsi. *Physical Review Letters*, 102(18):186602, 2009. 6, 67

[11] M. N. Wilson, M. Crisanti, C. Barker, A. Štefančič, J. S. White, M. T. Birch, G. Balakrishnan, R. Cubitt, and P. D. Hatton. Measuring the formation energy barrier of skyrmions in zinc-substituted cu2oseo3. *Physical Review B*, 99(17):174421, 2019. 6, 62

[12] W. Münzer, A. Neubauer, T. Adams, S. Mühlbauer, C. Franz, F. Jonietz, R. Georgii, P. Böni, B. Pedersen, M. Schmidt, A. Rosch, and C. Pfleiderer.

Skyrmion lattice in the doped semiconductor fe1-xcoxsi. *Physical Review B*, 81(4):041203, 2010. 6, 73

[13] L. J. Bannenberg, K. Kakurai, F. Qian, E. Lelièvre-Berna, C. D. Dewhurst, Y. Onose, Y. Endoh, Y. Tokura, and C. Pappas. Extended skyrmion lattice scattering and long-time memory in the chiral magnet fe1-xcoxsi. *Physical Review B*, 94(10):104406, 2016. 6

[14] Koya Makino, Johannes D. Reim, Daiki Higashi, Daisuke Okuyama, Taku J. Sato, Yusuke Nambu, Elliot P. Gilbert, Norman Booth, Shinichiro Seki, and Yoshinori Tokura. Thermal stability and irreversibility of skyrmion-lattice phases in cu2oseo3. *Physical Review B*, 95(13):134412, 2017. 6, 78

[15] T. Adams, A. Chacon, M. Wagner, A. Bauer, G. Brandl, B. Pedersen, H. Berger, P. Lemmens, and C. Pfleiderer. Long-wavelength helimagnetic order and skyrmion lattice phase in cu2oseo3. *Physical Review Letters*, 108(23):237204, 2012. 6

[16] L. J. Bannenberg, F. Qian, R. M. Dalgliesh, N. Martin, G. Chaboussant, M. Schmidt, D. L. Schlagel, T. A. Lograsso, H. Wilhelm, and C. Pappas. Reorientations, relaxations, metastabilities, and multidomains of skyrmion lattices. *Physical Review B*, 96(18):184416, 2017. 6, 61, 78

[17] Akira Tonomura, Xiuzhen Yu, Keiichi Yanagisawa, Tsuyoshi Matsuda, Yoshinori Onose, Naoya Kanazawa, Hyun Soon Park, and Yoshinori Tokura. Real-space

observation of skyrmion lattice in helimagnet mnsi thin samples. *Nano Letters*, 12(3):1673–1677, 2012. 7, 9, 65, 67

[18] X. Z. Yu, N. Kanazawa, Y. Onose, K. Kimoto, W. Z. Zhang, S. Ishiwata, Y. Matsui, and Y. Tokura. Near room-temperature formation of a skyrmion crystal in thin-films of the helimagnet fege. *Nat Mater*, 10(2):106–9, 2011. 7

[19] X. Z. Yu, Y. Onose, N. Kanazawa, J. H. Park, J. H. Han, Y. Matsui, N. Nagaosa, and Y. Tokura. Real-space observation of a two-dimensional skyrmion crystal. *Nature*, 465(7300):901–904, 2010. 7

[20] Wanjun Jiang, Gong Chen, Kai Liu, Jiadong Zang, Suzanne G. E. te Velthuis, and Axel Hoffmann. Skyrmions in magnetic multilayers. *Physics Reports*, 704:1–49, 2017. 9

[21] M. T. Birch, D. CortÃ©s-OrtuÃ±o, L. A. Turnbull, M. N. Wilson, F. GroÃŸ, N. TrÃ¤ger, A. Laurenson, N. Bukin, S. H. Moody, M. Weigand, G. SchÃ¼tz, H. Popescu, R. Fan, P. Steadman, J. A. T. Verezhak, G. Balakrishnan, J. C. Loudon, A. C. Twitchett-Harrison, O. Hovorka, H. Fangohr, F. Y. Ogrin, J. GrÃ¤fe, and P. D. Hatton. Real-space imaging of confined magnetic skyrmion tubes. *Nature Communications*, 11(1):1726, 2020. 9, 15

[22] S. Seki, J. H. Kim, D. S. Inosov, R. Georgii, B. Keimer, S. Ishiwata, and Y. Tokura. Formation and rotation of skyrmion crystal in the chiral-lattice insulator cu2oseo3. *Physical Review B*, 85(22):220406, 2012. 9

[23] Albert Fert, Nicolas Reyren, and Vincent Cros. Magnetic skyrmions: advances in physics and potential applications. *Nature Reviews Materials*, 2(7), 2017. 9, 30

[24] S. A. Montoya, S. Couture, J. J. Chess, J. C. T. Lee, N. Kent, M. Y. Im, S. D. Kevan, P. Fischer, B. J. McMorran, S. Roy, V. Lomakin, and E. E. Fullerton. Resonant properties of dipole skyrmions in amorphous fe/gd multilayers. *Physical Review B*, 95(22):224405, 2017. 11, 27, 31, 48

[25] J. Chadwick. Possible existence of a neutron. *Nature*, 129(3252):312–312, 1932. 12

[26] Tapan Chatterji. *CHAPTER 1 - Magnetic Neutron Scattering*, pages 1–24. Elsevier Science, Amsterdam, 2006. 12

[27] G. R. Ringo. *Neutron Diffraction and Interference*, pages 552–642. Springer Berlin Heidelberg, Berlin, Heidelberg, 1957. 12

[28] Y. Tokunaga, X. Z. Yu, J. S. White, H. M. Rønnow, D. Morikawa, Y. Taguchi, and Y. Tokura. A new class of chiral materials hosting magnetic skyrmions beyond room temperature. *Nature Communications*, 6, 2015. 15

[29] B. P. Toperverg. Specular reflection and off-specular scattering of polarized neutrons. *Physica B: Condensed Matter*, 297(1):160–168, 2001. 21

[30] Charles F. Majkrzak, Christopher Metting, Brian B. Maranville, Joseph A. Dura, Sushil Satija, Terrence Udovic, and Norman F. Berk. Determination

of the effective transverse coherence of the neutron wave packet as employed in reflectivity investigations of condensed-matter structures. i. measurements. *Physical Review A*, 89(3):033851, 2014. 21, 41

[31] 2017. 21

[32] H. J. C. Lauter, V. Lauter, and B. P. Toperverg. *Reflectivity, Off-Specular Scattering, and GI-SAS*, pages 411–432. Elsevier, 2012. 23, 34, 35

[33] Tetyana Kyrey, Marina Ganeva, Kornelia Gawlitza, Judith Witte, Regine von Klitzing, Olaf Soltwedel, Zhenyu Di, Stefan Wellert, and Olaf Holderer. Grazing incidence sans and reflectometry combined with simulation of adsorbed microgel particles. *Physica B: Condensed Matter*, 551:172–178, 2018. 23, 34, 45

[34] C. D. Graham B. D. Cullity. *Experimental Methods*, pages 23–86. John Wiley Sons, Ltd, 2008. 23

[35] Michael Donahue. Oommf user's guide, version 1.0. Report, 6376, National Institute of Standards and Technology, Gaithersburg, MD, 1999-09-01 1999. 25, 36

[36] S. X. Huang, Fei Chen, Jian Kang, Jiadong Zang, G. J. Shu, F. C. Chou, and C. L. Chien. Unusual magnetoresistance in cubic b20 fe0.85co0.15si chiral magnets. *New Journal of Physics*, 18(6):065010, 2016. 28, 63, 84

[37] T. Y. Ou-Yang, G. J. Shu, C. D. Hu, and F. C. Chou. Dynamic susceptibility study on the skyrmion phase stability of fe0.7co0.3si. *Journal of Applied Physics*, 117(12):123903, 2015. 28, 63

[38] Jan-Willem G. Bos, Claire V. Colin, and Thomas T. M. Palstra. Magnetoelectric coupling in the cubic ferrimagnet cu2oseo3. *Physical Review B*, 78(9):094416, 2008. 28

[39] S. A. Montoya, S. Couture, J. J. Chess, J. C. T. Lee, N. Kent, D. Henze, S. K. Sinha, M. Y. Im, S. D. Kevan, P. Fischer, B. J. McMorran, V. Lomakin, S. Roy, and E. E. Fullerton. Tailoring magnetic energies to form dipole skyrmions and skyrmion lattices. *Physical Review B*, 95(2):024415, 2017. 31

[40] Ivan Lemesh and Geoffrey S. D. Beach. Twisted domain walls and skyrmions in perpendicularly magnetized multilayers. *Physical Review B*, 98(10):104402, 2018. 31

[41] D. A. Gilbert, J. W. Liao, B. J. Kirby, M. Winklhofer, C. H. Lai, and K. Liu. Magnetic yoking and tunable interactions in fept-based hard/soft bilayers. *Sci Rep*, 6:32842, 2016. 31

[42] Nan Tang, Jung-Wei Liao, Siu-Tat Chui, Timothy Ziman, Alexander J. Grutter, Kai Liu, Chih-Huang Lai, Brian J. Kirby, and Dustin A. Gilbert. Controlling magnetic configuration in softâ€“hard bilayers probed by polarized neutron reflectometry. *APL Materials*, 10(1):011107, 2022. 31

[43] William Legrand, Jean-Yves Chauleau, Davide Maccariello, Nicolas Reyren, Sophie Collin, Karim Bouzehouane, Nicolas Jaouen, Vincent Cros, and Albert Fert. Hybrid chiral domain walls and skyrmions in magnetic multilayers. *Science Advances*, 4(7):eaat0415, 2018. 31

[44] Hyun Soon Park, Xiuzhen Yu, Shinji Aizawa, Toshiaki Tanigaki, Tetsuya Akashi, Yoshio Takahashi, Tsuyoshi Matsuda, Naoya Kanazawa, Yoshinori Onose, Daisuke Shindo, Akira Tonomura, and Yoshinori Tokura. Observation of the magnetic flux and three-dimensional structure of skyrmion lattices by electron holography. *Nature Nanotechnology*, 9(5):337–342, 2014. 33

[45] C. F. Majkrzak. Polarized neutron reflectometry. *Physica B: Condensed Matter*, 173(1):75–88, 1991. 33

[46] Shirin Nouhi, Maja S. Hellsing, Vassilios Kapaklis, and Adrian R. Rennie. Grazing-incidence small-angle neutron scattering from structures below an interface. *Journal of applied crystallography*, 50(Pt 4):1066–1074, 2017. 33

[47] M. -C Langner, S. Roy, S. -K Mishra, J. -C -T Lee, X. -W Shi, M. -A Hossain, Y. D. Chuang, S. Seki, Y. Tokura, S. -D Kevan, and R. -W Schoenlein. Coupled skyrmion sublattices in cu2oseo3. *Physical Review Letters*, 112(16):167202, 2014. 33, 78

[48] Dustin A. Gilbert, Brian B. Maranville, Andrew L. Balk, Brian J. Kirby, Peter Fischer, Daniel T. Pierce, John Unguris, Julie A. Borchers, and Kai Liu.

Realization of ground-state artificial skyrmion lattices at room temperature. *Nature Communications*, 6(1):8462, 2015. 33, 35, 36, 41, 42

[49] J. F. Ankner and G. P. Felcher. Polarized-neutron reflectometry. *Journal of Magnetism and Magnetic Materials*, 200(1):741–754, 1999. 34

[50] G. L. Squires. *Introduction to the Theory of Thermal Neutron Scattering*. Cambridge University Press, Cambridge, 3 edition, 2012. 35

[51] R. M. Moon, T. Riste, and W. C. Koehler. Polarization analysis of thermal-neutron scattering. *Physical Review*, 181(2):920–931, 1969. 35

[52] Brian Maranville, William Ratcliff II, and Paul Kienzle. reductus: a stateless python data reduction service with a browser front end. *Journal of Applied Crystallography*, 51(5):1500–1506, 2018. 35

[53] Dustin A. Gilbert, Alexander J. Grutter, Paul M. Neves, Guo-Jiun Shu, Gergely Zimanyi, Brian B. Maranville, Fang-Cheng Chou, Kathryn Krycka, Nicholas P. Butch, Sunxiang Huang, and Julie A. Borchers. Precipitating ordered skyrmion lattices from helical spaghetti and granular powders. *Physical Review Materials*, 3(1):014408, 2019. 38, 77

[54] R. C. Taylor and A. Gangulee. Magnetization and magnetic anisotropy in evaporated gdco amorphous films. *Journal of Applied Physics*, 47(10):4666–4668, 2008. 41, 48

[55] A. Singh, M. K. Sanyal, J. C. T. Lee, J. J. Chess, R. Streubel, S. A. Montoya, M. K. Mukhopadhyay, B. J. McMorran, E. E. Fullerton, P. Fischer, S. D. Kevan, and S. Roy. Discretized evolution of solitons in the achiral stripe phase of a fe/gd thin film. *Physical Review B*, 105(9):094423, 2022. 43

[56] Dustin A. Gilbert, Liang-Wei Wang, Timothy J. Klemmer, Jan-Ulrich Thiele, Chih-Huang Lai, and Kai Liu. Tuning magnetic anisotropy in (001) oriented l10 (fe1 xcux)55pt45 films. *Applied Physics Letters*, 102(13):132406, 2013. 48

[57] M. D. Kuz'min. Shape of temperature dependence of spontaneous magnetization of ferromagnets: Quantitative analysis. *Physical Review Letters*, 94(10):107204, 2005. 48

[58] Charles, Markus, Peter, Zakutna Dominika, Honecker Dirk, Dresen Dominique, Mees Flore, and Disch Sabrina. Sub-millisecond time-resolved small-angle neutron scattering measurements at nist. *Journal of Applied Crystallography*, 2020. 63

[59] Steven Kline. Reduction and analysis of sans and usans data using igor pro. *Journal of Applied Crystallography*, 39(6):895–900, 2006. 65

[60] K. Ishimoto, Y. Yamaguchi, J. Suzuki, M. Arai, M. Furusaka, and Y. Endoh. Small-angle neutron diffraction from the helical magnet fe0.8co0.2si. *Physica B: Condensed Matter*, 213-214:381–383, 1995. 73

[61] S. V. Grigoriev, S. V. Maleyev, V. A. Dyadkin, D. Menzel, J. Schoenes, and H. Eckerlebe. Principal interactions in the magnetic system fe1-xcoxsi: Magnetic structure and critical temperature by neutron diffraction and squid measurements. *Physical Review B*, 76(9):092407, 2007. 73, 84

[62] P. Bak and M. H. Jensen. Theory of helical magnetic structures and phase transitions in mnsi and fege. *Journal of Physics C: Solid State Physics*, 13(31):L881–L885, 1980. 73

[63] O. Nakanishi, A. Yanase, A. Hasegawa, and M. Kataoka. The origin of the helical spin density wave in mnsi. *Solid State Communications*, 35(12):995–998, 1980. 73

[64] N. Ogawa, S. Seki, and Y. Tokura. Ultrafast optical excitation of magnetic skyrmions. *Scientific Reports*, 5(1):9552, 2015. 78

[65] A. Chacon, L. Heinen, M. Halder, A. Bauer, W. Simeth, S. Mühlbauer, H. Berger, M. Garst, A. Rosch, and C. Pfleiderer. Observation of two independent skyrmion phases in a chiral magnetic material. *Nature Physics*, 14(9):936–941, 2018. 78

[66] Naoya Kanazawa, Shinichiro Seki, and Yoshinori Tokura. Noncentrosymmetric magnets hosting magnetic skyrmions. *Advanced Materials*, 29(25):1603227, 2017. 82

[67] E. A. Karhu, U. K. RÃ¶ÃŸler, A. N. Bogdanov, S. Kahwaji, B. J. Kirby, H. Fritzsche, M. D. Robertson, C. F. Majkrzak, and T. L. Monchesky. Chiral

modulations and reorientation effects in mnsi thin films. *Physical Review B*, 85(9):094429, 2012. 84

[68] G. Butenko, J. van den Brink, and R. Stamps. *Phenomenological Theory of Chiral States in Magnets with Dzyaloshinskii-Moriya Interactions.* Saechsische Landesbibliothek- Staats- und Universitaetsbibliothek Dresden, 2013. 84

[69] D. Schroeter, N. Steinki, M. Schilling, A. FernÃ¡ndez Scarioni, P. Krzysteczko, T. Dziomba, H. W. Schumacher, D. Menzel, and S. SÃ¼llow. Mnsi nanostructures obtained from epitaxially grown thin films: magnetotransport and hall effect. *Journal of Physics: Condensed Matter*, 30(23):235805, 2018. 84

[70] Ping Che, Ioannis Stasinopoulos, Andrea Mucchietto, Jianing Li, Helmuth Berger, Andreas Bauer, Christian Pfleiderer, and Dirk Grundler. Confined dipole and exchange spin waves in a bulk chiral magnet with dzyaloshinskii-moriya interaction. *Physical Review Research*, 3(3):033104, 2021. 84

[71] I. Stasinopoulos, S. Weichselbaumer, A. Bauer, J. Waizner, H. Berger, S. Maendl, M. Garst, C. Pfleiderer, and D. Grundler. Low spin wave damping in the insulating chiral magnet cu2oseo3. *Applied Physics Letters*, 111(3):032408, 2017. 84

[72] Balamurugan Balasubramanian, Priyanka Manchanda, Rabindra Pahari, Zhen Chen, Wenyong Zhang, Shahâ€‰R Valloppilly, Xingzhong Li, Anandakumar Sarella, Lanping Yue, Ahsan Ullah, Pratibha Dev, David A. Muller, Ralph

Skomski, George C. Hadjipanayis, and David J. Sellmyer. Chiral magnetism and high-temperature skyrmions in b20-ordered co-si. *Physical Review Letters*, 124(5):057201, 2020. 84

[73] P. M. Shepley, A. W. Rushforth, M. Wang, G. Burnell, and T. A. Moore. Modification of perpendicular magnetic anisotropy and domain wall velocity in pt/co/pt by voltage-induced strain. *Scientific Reports*, 5(1):7921, 2015. 87

[74] Hong Chul Choi, Shi-Zeng Lin, and Jian-Xin Zhu. Density functional theory study of skyrmion pinning by atomic defects in mnsi. *Physical Review B*, 93(11):115112, 2016. 87

[75] C.F. Majkrzak M. R. Fitzsimmons. *Application of polarized neutron reflectometry to studies of artificially structured magnetic materials*, pages 107–155. Springer US, Boston, MA, 2005. 113, 115

Appendix

Appendix A

Supplemental Materials For Neutron Scattering and Reflectometry

A.1 Scattering Length

The scattering of neutrons by a sample is characterized by changes in the energy and momentum of both incident and scattered neutrons. Consider a neutron with an incoming wavevector $\mathbf{k}_i$ and a scattered wavevector $\mathbf{k}_f$. The momentum transfer vector ($\mathbf{Q}$) can be expressed as the change in momentum ($\mathbf{P}$) according to Equation (A.1). Since we are only concerned with elastic scattering (where energy is conserved), the magnitude of $\mathbf{k}$ remains constant, depending on the neutron's wavelength.

$$\mathbf{P} = \hbar\mathbf{k}_i - \hbar\mathbf{k}_f = \hbar\mathbf{Q} \tag{A.1}$$

Here, the Planck constant is denoted as $\hbar = h/2\pi$, and $|\mathbf{k}| = 2\pi/\lambda$, where λ is the wavelength of the neutron.

In the context of neutrons as waves, we describe the incident wave as shown in Equation (A.2), and the scattered wave as shown in Equation (A.3). In the scattered wave equation, b is a constant that is independent of the scattered angle (2θ), and the minus sign is arbitrary, corresponding to a positive value of b for a repulsive potential. The quantity b has dimensions of length and is defined as the scattering length. It can be written as $b = b_0 + ib'$, where b_0 represents the length associated with the real component, indicating good scattering samples, and the imaginary component (b') represents neutron absorption by the nucleus. Some neutron-absorbing nuclei include ^{113}Cd, ^{157}Gd, etc. Experimental values for the parameter b can be found on the NIST website (Neutron scattering lengths and cross sections). Additionally, b varies irregularly with atomic number.

$$\Psi_{inc} = e^{\vec{k_i}\cdot\vec{z}} \tag{A.2}$$

$$\Psi_{sc} = -\frac{b}{r}e^{\vec{k_f}\cdot\vec{r}} \tag{A.3}$$

$$b = b_0 + \mathrm{i}b' \tag{A.4}$$

A.2 Differential Cross Section

To gain insight into where the incident neutrons are scattered into detectors, we must consider a specific solid angle defined by θ and ϕ. The rate of neutron detection on the detector depends on the solid angle ($\Delta\Omega$) and the detector efficiency (η), as given by Equation (A.5). In Equation (A.5), ϕ represents the flux of incident neutrons. The quantity $\left(\frac{\partial\sigma}{\partial\Omega}\right)$ is referred to as the differential cross-section, which is expressed per unit area. By following Fermi's golden rule, Equation (A.5) can be written as shown in Equation (A.6). Here, m denotes the mass of the neutron, and V represents the interaction potential between the neutron and the sample.

$$C = \Delta\Omega\eta\left(\frac{\partial\sigma}{\partial\Omega}\right)\phi \tag{A.5}$$

$$\left(\frac{\partial\sigma}{\partial\Omega}\right)_{\sigma_i,\lambda_i\rightarrow\sigma_f,\lambda_f} = \left(\frac{m}{2\pi\hbar^2}\right)^2 |\langle k_f, \sigma_f, \lambda_f|V|k_i, \sigma_i, \lambda_i\rangle|^2 \tag{A.6}$$

The scattering potential can be written as the sum of nuclear and magnetic potentials, as shown in Equation (A.7). In this equation, μ_n represents the neutron's

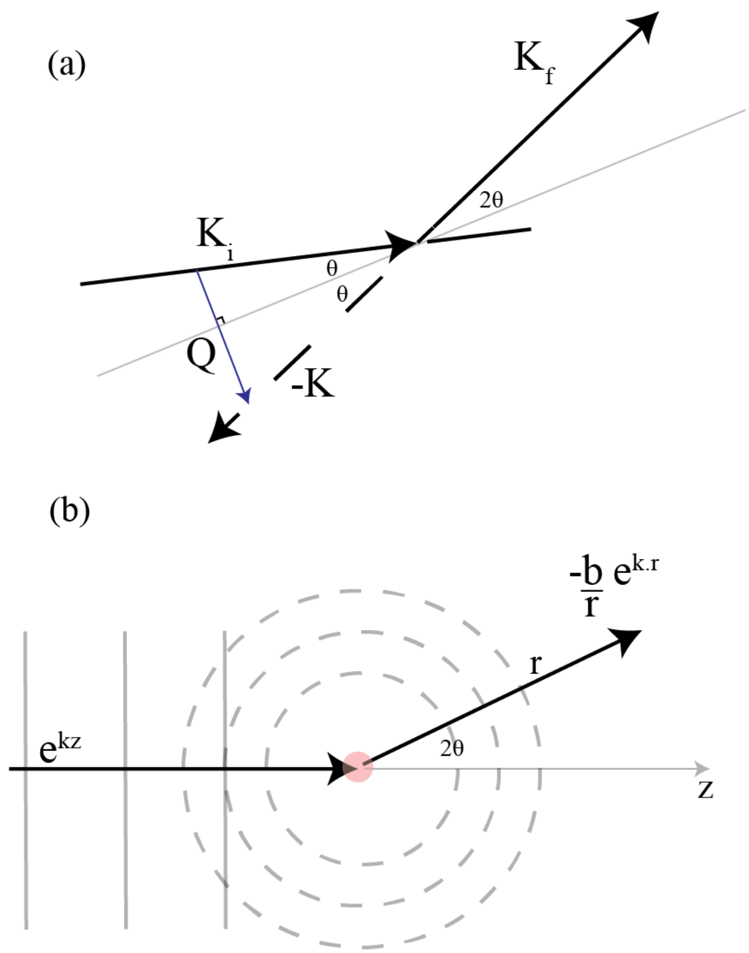

Figure A.1: (a) momentum transfer vetor in terms of incident and scattered wavevector (b) A plane wave of neutrons travelling in z direction and scattered uniformally from a stationary nuclei and scatter in radial direction.

magnetic moment. The nuclear potential in Equation (A.7) can be further expressed as shown in Equation (A.8), where b_i is the scattering length of the i^{th} atom.

$$V = V_n + V_m = V_n \mp \vec{\mu_n} \cdot \vec{B} \tag{A.7}$$

$$V_n = \frac{2\pi\hbar^2}{m} \sum_i b_i \tag{A.8}$$

The scattering lenght density (SLD) ρ can be introduced as A.9,

$$\rho = \sum_i^J N_i b_i \tag{A.9}$$

The quantity N_i defines the number density for distinct atoms.

A.3 Magnetic Scattering

Vector potential from an unpaired electron (A.2a) ($\vec{A_e}$) can be written as shown in Equation (A.10). In Equation (A.10), $\vec{\mu_e} = -2\mu_B \vec{s_e}$, where $\mu_B = \frac{e\hbar}{2m_e}$, and $\vec{s_e}$ are spin 1/2 operators. The dipolar field created by an unpaired electron ($\vec{B_e}$) is represented in Equation (A.11).

$$\vec{A_e} = \frac{\mu_0}{4\pi} \frac{\vec{\mu_e} \times \vec{r}}{|\vec{r}^3|} = \frac{\mu_0}{4\pi} \vec{\mu_e} \times \vec{\nabla} \frac{1}{|\vec{r}|} \tag{A.10}$$

(a)

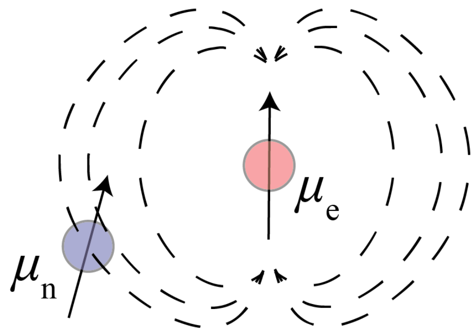

(b)

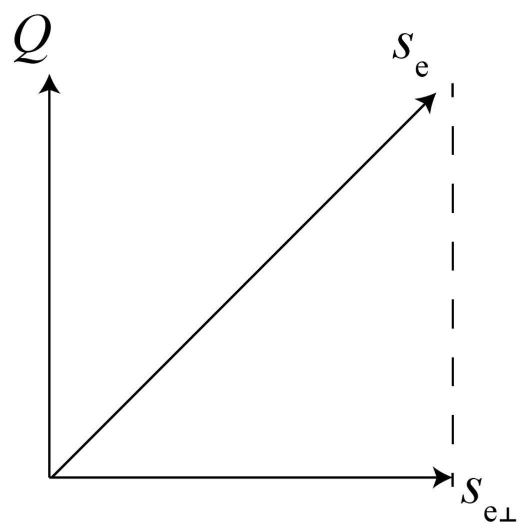

Figure A.2: (a) Dipole field generated from an unpaired electron (dashed lines). μ_e is the moment of the electron and μ_n is the moment associated with neutron (b) Schematic of spin of electron and its component perpendicular to the maomentum transfer vector (Q). adapted from (article)[4]

$$\vec{B}_e = \vec{\nabla} \times \vec{A}_e = \frac{\mu_0}{4\pi}\vec{\nabla} \times \left(\vec{\mu_e} \times \nabla \frac{1}{|\vec{r}|}\right) \tag{A.11}$$

We can reduce the the equation in A.6 to A.12, where $\vec{\sigma_n} = 2\vec{s_n}$ and $\vec{s_n}$ is the spin 1/2 operator for neutron.

$$\left(\frac{\partial \sigma}{\partial \Omega}\right)_{\sigma_i,\lambda_i \rightarrow \sigma_f,\lambda_f} \propto \left|\left\langle k_f, \lambda_f \middle| \vec{\sigma}_n \cdot \vec{\nabla} \times \left(\vec{s}_e \times \nabla \frac{1}{|\vec{r}|}\right) \middle| k_i, \lambda_i \right\rangle\right|^2 \tag{A.12}$$

we can further reduce these equation methods mentioned in (article) to the final form of A.13 indicating that neutrons sensitive to the magnetic moments perpendicular to the Q or the momentum transfer vector.

$$\left\langle \vec{k}_f \middle| \nabla \times \left(s_e \times \nabla \frac{1}{|\vec{r}|}\right) \middle| \vec{k}_i \right\rangle = 4\pi \underbrace{\hat{Q}_e\left(\vec{s}_e \times \hat{Q}\right)}_{\equiv \vec{S}_{e\perp}} \tag{A.13}$$

To generalize the eq.A.13 to an atom we can multiply the eq.A.13 by magnetic form factor of an atom, which is given by the equation A.14

$$f(\vec{Q}) = \frac{1}{2\mu_B} \int \mathcal{M}(\vec{r}) e^{-i\vec{Q}\cdot\vec{r}} \tag{A.14}$$

A.4 Polarized Neutron Reflectometry (PNR)

Reflectivity involves measurements of the reflected beam from a planner interfaces. This technique is intrinsically sensitive to the difference to the difference of the refractive index across interfaces [75]. From reflectometry we can obtain depth dependent average inplane scattering length density profiles of the sample.

to solve the neutron reflectometry, we apply time-independent Schrödinger equation to obtain a solution for the wave function, ψ, representing the neutron wave inside and outside of the reflecting sample.

$$\left[-\frac{\hbar^2}{2m}\nabla^2 + V\right]\psi = E\psi \tag{A.15}$$

since we talk about elastic scattering energy must be conserve.

$$\therefore \quad E_0 = E = \frac{\hbar^2 k^2}{2m} \tag{A.16}$$

Therefore the total energy can be written for inside the media as

$$\frac{\hbar^2 k^2}{2m} + \frac{2\pi\hbar^2}{m}\rho = \frac{\hbar^2 k_0^2}{2m} \tag{A.17}$$

Where V is defined by A.8 and equation can be further deduced to eq.A.18 and A.19. We assume the scattering potential in changing along the z direction.

$$k_0^2 = k^2 + 4\pi\rho_z \tag{A.18}$$

$$k = nk_0 = \sqrt{1 - \frac{4\pi\rho_z}{k_0^2}}k_0 \tag{A.19}$$

where n is the refractive index and momentum transfer vector defined by $Q = k - k_0$. In neutron reflectometry Q_c defined as the incident angle where the reflcted intensity becomes unity (total reflection). Above critical angle we can define the reflectivity by using born approximation defined by following eqaution.

$$R_{BA} \propto \frac{1}{Q_\perp^2} \left| \int_{-\infty}^{\infty} e^{iQ_\perp z} \rho(z) dz \right|^2 \tag{A.20}$$

A.4.1 Magnetic Dependent Reflectometry

BY stating with eq.A.7 we can rewrite the potential matrix notation.

$$V = \frac{2\pi\hbar^2}{m_n} \begin{pmatrix} \rho_n & 0 \\ 0 & \rho_n \end{pmatrix} \mp \mu_n \begin{pmatrix} B_z & B_x - iB_y \\ B_x + iB_y & -B_z \end{pmatrix} \tag{A.21}$$

Setting $\boldsymbol{B} = \mu_0 \boldsymbol{H} + \boldsymbol{M}$, where $\boldsymbol{M}$ is the intensity of magnetization, and for fields applied along $\hat{\boldsymbol{z}}$, eq.A.21 can be rewritten as:

$$V = \frac{2\pi\hbar^2}{m_n} \begin{pmatrix} \rho_n & 0 \\ 0 & \rho_n \end{pmatrix} \mp \mu_n \begin{pmatrix} M_z & M_x - iM_y \\ M_x + iM_y & -M_z \end{pmatrix} \tag{A.22}$$

Furthermore we can define magnetic scattering length density as,

$$\boldsymbol{\rho}_m = -\frac{m_n}{2\pi\hbar^2} \mu_n \sum_i^J \boldsymbol{M}_i \tag{A.23}$$

plug eq.A.23 into eq.A.22

$$V = \frac{2\pi\hbar^2}{m_n} \begin{pmatrix} \rho_n + \rho_{mz} & \rho_{mx} - i\rho_{my} \\ \rho_{mx} + i\rho_{my} & \rho_n - \rho_{mz} \end{pmatrix} \tag{A.24}$$

then we can define the four cross sections of PNR as,

$$\begin{aligned}
\rho_{++} &= \rho_n + \rho_{mz} \\
\rho_{--} &= \rho_n - \rho_{mz} \\
\rho_{+-} &= \rho_{mx} - i\rho_{my} \\
\rho_{-+} &= \rho_{mx} + i\rho_{my} \\
V &= \tfrac{2\pi\hbar^2}{m_n} \begin{pmatrix} \rho_{++} & \rho_{+-} \\ \rho_{-+} & \rho_{--} \end{pmatrix}
\end{aligned} \tag{A.25}$$

We can plug these potential in A.20 and get four differert cross (R++, R−−, R+− and R−+) for polarized neutron reflectivity.

Above derivatives are mentioned in [75] in more details

Appendix B

Supplemental Materials For Chapter 3

B.1 Hystersis Loop Data For FeGd ML System

Magnetometry data for Fe/Gd ML. Magnetometry data was measured using an out of plane magnetic field by using Quantum Design Dynacool PPMS.

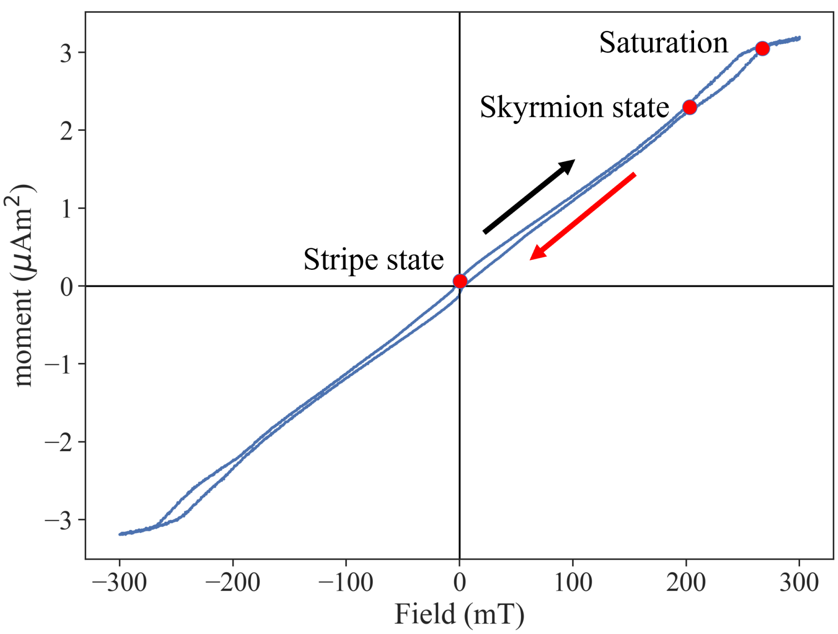

Figure B.1: The Fe/Gd ML system was characterized by measuring the magnetic moment vs field data. The sample was first saturated by applying a field of 500 mT at 45 degrees with respect to the out-of-plane (OOP) direction. Then the field was decreased, as indicated by the red arrow, until zero field (remanence) was reached, at which point a stripe state is formed (as evidenced by two diffraction peaks in the SANS detector). Subsequently, the field was increased to 190 mT in the OOP direction, as indicated by the black

Vita

W.L. Namila C Liyanage is from Sri Lanka. He attended Ananda College, Colombo in Sri Lanka. He graduated with a bachelor's degree from the University of Colombo with a Major in Physics in 2015. In 2017 he came to the USA to pursue doctoral studies in Physics at the University of Tennessee.